Applied Water Science (2022) 12:193
https://doi.org/10.1007/s13201-022-01713-4

ORIGINAL ARTICLE

A comparative optimization and modeling of ammonia–nitrogen adsorption from abattoir wastewater using a novel iron-functionalized crab shell

Paschal Enyinnaya Ohale[1] · Chijioke Elijah Onu[1] · Joseph Tagbo Nwabanne[1] · Chukwunonso Onyeka Aniagor[1] · Chinenye Faith Okey-Onyesolu[1] · Nonye Jennifer Ohale[1]

Received: 6 April 2021 / Accepted: 1 June 2022 / Published online: 1 July 2022

Abstract

High-grade adsorbent (Fe–CS) was successfully synthesized from waste crab shells (CS) for the adsorptive removal of ammonia–nitrogen (A–N) from abattoir wastewater. Fe–CS was analyzed using Fourier transform infrared spectroscopy, x-ray diffraction, Scanning electron microscopy, and Thermogravimetric analysis. The characterization results indicated that Fe–CS possessed important qualities required for surface-driven chelation. The analysis of variance result showed that Fe–CS dosage (with *f*–value of 284.5) was the most effective process parameter of influence during A-N adsorption. The regression coefficients obtained from the process modeling illustrated the applicability of RSM ($R^2 = 0.9799$), ANN ($R^2 = 0.9025$), and ANFIS ($R^2 = 0.9998$) in predicting the A–N adsorptive removal, while the comparative statistical analysis established the superiority of ANFIS model over ANN and RSMs' data prediction accuracy. The optimization result further demonstrated that ANFIS–GA predicted an optimum removal efficiency of 92.60% at pH of 6.5, a dosage of 2.2 g, A–N conc. of 18.8 mg/L, Temp. of 317 K, and adsorption time of 156 min. The mechanistic plot obtained from Weber–Morris model depicted that three regions were involved in the adsorption process. Boyd model parameters revealed that intraparticle diffusion controlled the process at low A–N concentration (A–N concentration ≤ 15 mg/L), while film diffusion dominated the adsorption process at concentrations higher than 15 mg/L. The average Gibbs free energy value ($-\Delta G^0 = 3.08212$ kJ/mol), enthalpy ($\Delta H^0 = 4.1150$ kJ/mol), activation energy ($E_A = 3.7454$ kJ/mol) and entropy ($\Delta S^0 = 22.9710$ J/mol K) obtained from thermodynamic studies confirmed the spontaneous, endothermic, favorable and physical nature of the process.

Keywords Artificial neural network · Characterization · Response surface methodology · Mechanistic studies · Slaughterhouse

Introduction

According to the Food and Agricultural Organization (FAO), freshwater is one of the most significant commodities required for the sustenance of human life. Meanwhile, the presence of organic and inorganic pollutants resulting from the unrestricted discharge of effluents from various industries (desalination, oil & gas, abattoir, etc.) significantly degrades water quality, thus, making it unsuitable for use as a direct source of potable water for industrial applications (Panagopoulos 2021). These issues have worsened the problem of freshwater scarcity over the last two decades (Panagopoulos 2022; Hashem et. al. 2021a).

Abattoir industries are very lucrative, especially in developing countries like Nigeria, as they provide a means to the major source of protein supply and also account for about 21% of the country's agricultural GDP (Ogbeide 2015). In addition to the nourishment and huge economic derivatives accruable from the abattoir industries, the issue of generation of a considerable volume of contaminated wastewaters (abattoir wastewater, AWW) during their operations still subsists. Studies have shown that these AWW are characterized by a variety of organic pollutants, which serve as substrates for ammonia–nitrogen (A-N) generating microorganisms (Elemile et al. 2019; Lin et al. 2014; Lopes et al. 2022). Due to the high toxicity of A-N, which has been extensively

✉ Paschal Enyinnaya Ohale
pe.ohale@unizik.edu.ng

[1] Department of Chemical Engineering, Nnamdi Azikiwe University, P.M.B. 5025, Awka, Nigeria

reported (Elemile et al. 2019; Haseena et al. 2016; Halim et al. 2010), their total elimination or considerable reduction in AWW is plausible.

Many techniques such as chemical precipitation, nitrification and denitrification, electrochemical coagulation, and membrane distillation (Haseena et al. 2016; Halim et al. 2010; Chen et al. 2018; Jorgensen et al. 2003; Mao et al. 2018; Qiang et al. 2020) have been successfully adopted for the removal of A-N from different sources. The reliability of adsorption techniques for A-N removal from AWW is attributed to the operational flexibility, cost-effectiveness, fast kinetics, and it is insensitive to ammonia toxicity as highlighted by several authors (Mao et al. 2018; Qiang et al. 2020; Ren et al. 2021; Mirahsani et al. 2019). Different adsorbents such as cross-linked chitosan, activated carbon and sawdust, etc., have been applied for AWW treatment (Atangana and Chiweshe 2019; Agarry and Owabor 2012; Djonga et al. 2019). However, this study evaluated the effectiveness of crab shell-based adsorbent for the chelation of A-N from AWW.

Composed mainly of calcium carbonate, chitin, and proteins (Jeon et al. 2019; Ohale et al. 2020), the properties of crab shell biosorbent are linked to their rigid structure, high mechanical strength, and ability to withstand extreme conditions employed during the synthesis and adsorption process (Jeon et al. 2019). Jeon et al. (2019) and Jeon (2015), studied the removal of chromium and silver ions from an aqueous solution, using amino-functionalized crab shell and immobilized crab shell beads. Using crab shell particles, Vijayaraghavan et al. (2011), investigated the removal of Mn (II) and Zn (II) from aqueous solutions. Also, iron functionalized activated carbon was successfully applied for the uptake of aqueous silver (Wang et al. 2019). Currently, the removal of A-N has focused on its adsorption from municipal wastewater sources (Qiang et al. 2020; Cheng et al. 2019). However, to our best knowledge, no work has been published on the adsorptive removal of A-N from AWW using crab shells, thus making this work imperative.

In the past, a uni-variant procedure (OFAT) was commonly adopted for evaluating the adsorptive removal of A-N (Hodur et al. 2020; Wang et al. 2018; Arslan and Veli 2011). However, OFAT approach is usually cumbersome, time-consuming, and rarely satisfies the search for the desired optimum. Using multi-variant empirical techniques which examine the simultaneous variations of process factors on the response, the limitations of the OFAT technique can be circumvented (Onu et al. 2020). Many nonlinear analytical techniques have been previously applied for nonlinear system modeling (Betiku et al. 2018, 2016), but response surface methodology (RSM), artificial neural network (ANN), and adaptive neuro-fuzzy inference system (ANFIS) have consistently shown good modeling and simulation results (Chen et al. 2015; Myers et al. 2009). RSM and ANN are flexible mathematical tools, and artificial intelligence (AI) algorithms, respectively, used for the design, modeling and optimization of majorly nonlinear systems (Chen et al. 2015; Ohale et al. 2017). Literature has documented evidence of researchers' strong preference for ANN in data modeling in comparison with RSM (Wang et al 2018; Tu et al. 2019). This finding may not be unconnected with its (ANN) prediction accuracy, and minimal modeling data requirement (so long the data are statistically well distributed in the input domain) (Mahanty et al. 2020; Hariram et al. 2019; Dehghani et al. 2019; Dehghani et al. 2020).

Comparative assessment of ANN and RSM (Onu et al 2020; Betiku et al. 2018; Ohale et al. 2017), as well as those between ANN and ANFIS (Onu et al. 2021a; Dastorani et al. 2010; Kiran and Rajput 2011) in process modeling, has been reported by several authors. While some authors have verified the dominance of both ANN and ANFIS over RSM (Onu et al. 2020, 2021a, 2021b), Taheri et al. (2013) and Sajjadi et al. (2016) reported that RSM performed better than ANFIS. Furthermore, Kiran and Rjput (2011) observed that ANN performed better than ANFIS, even as Dastorani et al. (2010) confirmed the superiority of ANFIS over ANN. Betiku et al. (2016) established that both ANFIS and ANN were better than RSM, whereas ANN was slightly superior to ANFIS in data prediction accuracy. These inconsistent reports underscore the need to compare the predictive fitness of RSM, ANN and ANFIS under identical conditions, particularly as it relates to A–N uptake from AWW. Regardless of the numerous comparative applications of RSM, ANN and ANFIS in modeling of different processes (Zarghi et al. 2020; Ting et al. 2020; Arabameri et al. 2015), no article exists on their application in the removal of A–N. This observation forms a major motivation for the work; hence, this present work is justified.

Therefore, the study aims at synthesizing a novel iron-functionalized crab shell-based adsorbent with high A-N uptake capacity via thermal and chemical (impregnation) activation methods. Iron was chosen as a modifying agent owing to its special properties, namely catalysis, reduction, and increased electron transfer efficiency, which can improve the properties of CS with a larger surface area (Qin et al. 2020; Lyu et al. 2019). The pre- and post-adsorption characteristics of the synthesized novel adsorbent obtained, as well as the synergistic effects of process variables, were evaluated using RSM, ANN and ANFIS. Using genetic algorithm and RSM, the adsorptive system was further optimized, while the probable rate-controlling step and thermodynamics considerations during adsorptive uptake were elucidated.

Experimental

Materials

Crabshell was obtained from a waste disposal site in Badagry, Lagos State, Nigeria. The shells were washed and dried at a temperature of 378 K. With the aid of a mill apparatus, the dried shells were powdered and sieved to pass through 0.2 mm mesh size and subsequently stored in an airtight container for further processing.

Abattoir wastewater (AWW) was obtained from a local slaughterhouse in Amasea, Anambra state, Nigeria. AWW was characterized following standard procedures for water and wastewater analysis (APHA 2005; AWWA 2005), and the results are presented in Table 4. The characterized AWW was filtered to remove all solid particles capable of clogging the surface of the adsorbent and subsequently preserved in a dark-amber colored container for further analysis.

Analytical grade reagents of sulfuric acid (H_2SO_4), sodium hydroxide (NaOH), and iron nitrate (Fe $(NO_3)_3$) were purchased from Parchem limited, New Rochelle, New York, USA.

Adsorbent preparations

Fifty grams of ground crab shell was contacted with 400 ml of 0.3 M $Fe(NO_3)_3$ at 318 K for 7 h. The product was thoroughly washed with deionized water to remove all residual traces of the chemical. After drying, the chemically active crab shell was calcined for 3 h in a muffle furnace at 593 K, and the resultant product (iron-functionalized crab shell, Fe–CS) was cooled and stored for further use.

Instrumental characterization

Physicochemical properties of crab shell (CS), Fe–CS, and A–N-loaded Fe–CS were investigated using instrumental characterization. The functional groups, topographical equilibrium and crystalline structure of the samples were determined via Fourier transform infrared spectroscopy (FTIR – Thermo Nicolet Nexus, Model 470/670/870), scanning electron microscopy (SEM – Model Zeiss Evo MA – 17 EDX/WDS microscopy), and X-ray diffraction (XRD – Philips XPERT X-RAY diffraction unit), respectively. Additionally, the thermal strength was analyzed by thermogravimetric analysis (TGA – Mettler Toledo TGA/SDTG 851). FTIR, XRD, SEM, and TGA analyses were carried out following ASTM E1421–99, ASTM F1185–88, ASTM E2809, and ASTM D3418 standard procedure, respectively.

Adsorption studies

The A–N removal efficiency was investigated at varying pH (4, 5, 7, 9, 10), Fe-CS dosages (0.7, 1.0, 1.6, 2.2, 2.5 g), initial A–N concentrations (1.7, 16.0, 44.5, 73.0, 87.5 mg/L), temperature (305.5, 308.0, 313.0, 318.0, 320.5 ^{o}K), and time (30, 60, 120, 180, 210 min). The experimental template (see Table S1) comprises 32 sets of individual runs, whose uniqueness lies in their input parameters synergy. The solution pH was adjusted with adequate drops of 0.5 M H_2SO_4 and 0.6 M NaOH and standardized with Hanna pH instruments (Model H12002–02). After pH adjustment, desired amounts of Fe–CS were added to 50 ml of AWW, and the mixture was stirred at 180 rpm for the specified adsorption time. The Fe–CS/AWW mixture obtained at the end ofcc each experimental run was separated by centrifugation and the supernatant was withdrawn for A–N analysis, while the spent Fe–CS adsorbate was recovered for characterization.

The experimental kinetic data used for mechanistic modeling was obtained by studying the effect of time (15–300 min) and concentration (15.0–75.0 mg/L) on the A–N adsorption capacity (q_t). The result of this study is illustrated in supplementary material. The equilibrium A–N concentration was determined by Nessler's Reagent spectrophotometry, while removal efficiency and adsorption capacity were determined using Eq. (1) and Eq. (2), respectively.

$$A-Nremovaleff.(\%)=\frac{C_0-C_t}{C_0}(100) \tag{1}$$

$$q_t=\frac{C_0-C_t}{m}V \tag{2}$$

C_0 = Initial concentration of A–N (mg/L), C_t = residual concentration of A–N (mg/L), V = volume of AWW per batch (L), m = mass of Fe–CS (g) and q_t = adsorption capacity at time, t (mg/g).

Predictive and mechanistic modeling

RSM

The literature review showed the dependence of A-N removal efficiency on five process variables (pH, adsorbent dosage, initial concentration, adsorption temperature, and contact time) (Ren et al. 2021; Tu et al. 2019; Li et al. 2020; Couto et al. 2016; Kizito et al. 2015; Hodur et al. 2020; Wang et al. 2018; Arslan et al. 2011). The RSM–Central Composite Design provides the process variables' synergistic study framework using an optimal number of experimental runs. Given that all the parameters are measurable, the mathematical relationship between

independent variables and removal efficiency is expressed by the second-order polynomial function (Eq. 3). To estimate the statistical significance of each term in the polynomial function, the independent variables and corresponding responses were analyzed using analysis of variance, ANOVA (Table 5) (Betiku et al. 2018; Ohale et al. 2017).

$$y = b_0 + \sum b_i X_i + \sum b_{ii} X_{ii} + \sum b_{ij} X_i X_j + \varepsilon \tag{3}$$

For statistical analysis, the experimental variable has been coded as shown in Eq. 4:

$$x_i = \frac{X_i - X_n}{\Delta X_i} \tag{4}$$

where x_i is the coded value of i_{th} independent variable, X_i is the actual value of the i_{th} independent variable, x_n is the actual value of i_{th} independent variable at the center point and, ΔX is the step change value of a real variable (Betiku et al. 2018; Ohale et al. 2017). The design matrix (Table S1) is generated based on five level input parameters given in Table 1 and the response surface methodology was carried out using the Design-Expert software 11.0 trial version (Stat-Ease Inc., Minneapolis, USA).

ANN

Multi-Layer Perceptron (MLP), aided with Marquardt Levenberg's backpropagation algorithm, was used in developing the ANN. The MLP consists of five input variables making up the input layer, with the A–N removal efficiency representing the output neuron (See Fig. 1a). Neuron input consists of its bias and the sum of its weighted input. The mathematical expression describing the neuron is given in Eq. 6, while the data set employed in ANN modeling was the same as those used in RSM (see Table S1). Seventy per cent (70%) of the data set was used for network training, while the remaining 30% was evenly used for validation and testing set (Ohale et al. 2017). To eliminate the influence of large–value process variables, all input parameters and responses were normalized using Eq. 5. The ANN was executed in MATLAB R 2015 b (Mathworks, Inc.).

$$X_{norm.} = \frac{X_i - X_{\min.}}{X_{\max.} - X_{\min.}} \tag{5}$$

$$Y_i = \sum_{i=1}^{n} x_i \omega_i + \theta_i \tag{6}$$

where $X_{norm.}$ represents the normalized value of X_i, $X_{\min.}$ and $X_{\max.}$ denotes the minimum and the maximum values of the data set. The Y_i is the net input to the node, i is the hidden layer, $\omega_i (i = 1, n)$ denotes the connection weights, θ_i represents the bias and x_i is the input parameter.

The weighted output was subjected to a nonlinear activation function (Tu et al. 2019), while the logistic output function is given in Eq. (7).

$$sf(sum) = \frac{1}{1 + \exp(-sum)} \tag{7}$$

The hidden number of neurons was arbitrarily varied from 2.0 to 12.0, and a suitable number of the hidden neuron was chosen based on the results of regression and error function analysis obtained by applying Eqs. (8) and (9). Meanwhile, the graphical result of this test is presented in Fig. 5e.

$$R^2 = 1 - \frac{\sum_{i=1}^{N} \left(y_{\exp.(i)} - y_{\text{pred.}(i)}\right)^2}{\sum_{i=1}^{N} \left(y_{\text{pred.}(i)} - y_{\exp.ave.}\right)^2} \tag{8}$$

$$\text{RMSE} = \sqrt{\frac{\sum_{i=1}^{N} \left(y_{\text{pred.}(i)} - y_{\exp.(i)}\right)^2}{N}} \tag{9}$$

where N is the number of data points, $y_{\text{pred.}(i)}$ is the ANN prediction, $y_{\exp.(i)}$ is the actual experimental response, $y_{\exp.ave.}$ is the mean value of experimental data and i is the data index (Onu et al. 2020).

ANFIS

A fuzzy model for the prediction of A–N removal efficiency was initiated using a feed-forward neural network structure. The network consists of a multi-input single-output (MISO) ANFIS model which was developed using the fuzzy logic toolbox of MATLAB R 2015 b (Mathworks Inc.). The

Table 1 Levels of independent variables for central composite design

Factors	Unit	Symbol	Coded variable levels				
			−1.5	−1	0	1	1.5
pH		x_1	4	5	7	9	10
Dosage	*g*	x_2	0.7	1	1.6	2.2	2.5
A–N Conc	mg/L	x_3	1.75	16	44.5	73	87.25
Temp	*K*	x_4	305.5	308	313	318	320.5
Time	minutes	x_5	30	60	120	180	210

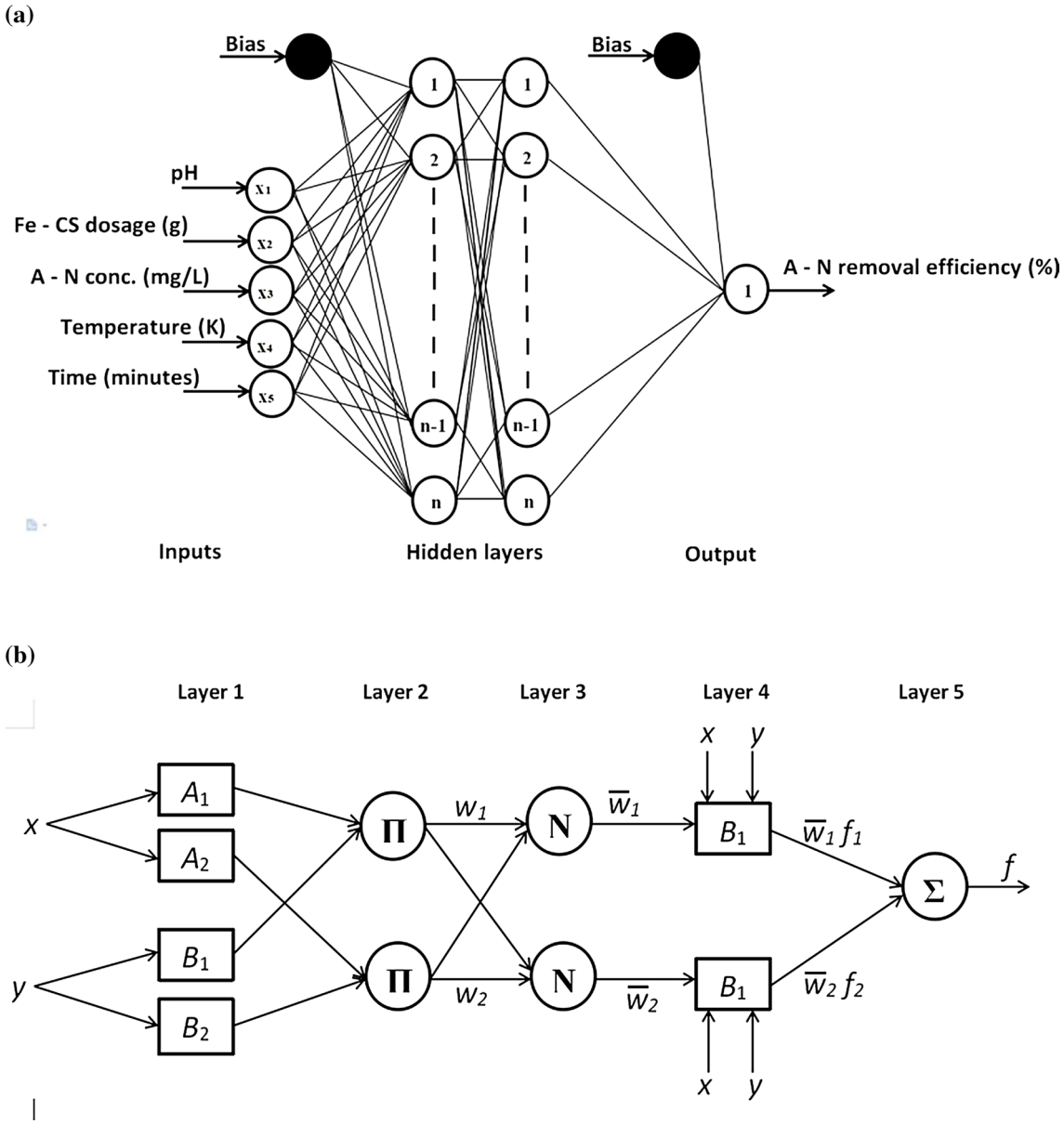

Fig. 1 Architectural framework of **a** ANN **b** ANFIS

architectural framework of the suggested ANFIS model, whose structure involved five discrete layers (Betiku et al. 2016) is presented in Fig. 1b. First-order Sugeno inference systems that convert input parameters into membership functions (MF) were employed for this investigation. To further analyze the ANFIS framework presented in Fig. 1b, the fuzzy inference system was assumed to have two input variables (x, y) and one output (f), as a result, the fuzzy 'IF–THEN' rules apply as expressed in Eqs. (10) and (11) (Betiku et al. 2016; Betiku et al. 2018).

$$\text{Rule 1 : IF} x \text{ is} A_1 \text{ and} y \text{ is} B_1, \text{ then} f_1 = k_1 x + l_1 y + m_1 \quad (10)$$

$$\text{Rule 1 : IF} x \text{ is} A_2 \text{ and} y \text{ is} B_2, \text{ then} f_2 = k_2 x + l_2 y + m_2 \quad (11)$$

where A_i and B_i are fuzzy sets, f_i is output, k_i, l_i and m_i are adjustable parameters set during ANFIS training [38]. Five layers of the ANFIS model were explained via Eqs. (12)–(16).

Layer 1 All nodes (i) in the first layer are defined by the function in Eq. (12).

$$O_i^1 = \mu_{A_i}(x) \quad (12)$$

where x is the input node, i and O_i^1 are the membership grade of fuzzy set A_i.

Layer 2 Every node i approximates the weight of each membership function (MF) by way of multiplication (Betiku et al. 2018), as shown in Eq. (13).

$$O_i^2 = w_i = \mu_{A_i}(x) * \mu_{B_i}(y); [i = 1, 2] \tag{13}$$

Layer 3 In this third layer, the approximated MFs are normalized by computing each activation level using Eq. (14).

$$O_i^3 = w_i = \frac{w_i}{w_i + w_2}, [i = 1, 2] \tag{14}$$

Layer 4 The fourth layer is used to compute the output by de-fuzzing the MFs via Eq. (15).

$$O_i^4 = \overline{w_i} * f_i = \overline{w_i}\left(k_i * x * l_i * y + m_i\right) \tag{15}$$

where $\overline{w_i}$ is the output of the third layer and k_i, l_i, and m_i are parameter set.

Layer 5 The fifth layer is a single non-adaptive node used to compute the overall output using Eq. (16).

$$O_i^5 = \sum_i \overline{w_i} * f_i = \frac{\sum_i w_i * f_i}{\sum_i w_i} \tag{16}$$

Appraisal of predictive models

To ascertain the superiority of either ANN, RSM, or ANFIS in predicting the A-N removal efficiency, the respective model predictions were compared using error function indices (such as regression coefficient, R; coefficient of determination, R^2; adjusted–R^2, absolute average relative error, AARE; % Marquardt's percent standard deviation, MPSED; root-mean-square error, RMSE; standard deviation, SD; the sum of squares error, SSE and Hybrid fractional error function HYBRID %) (Onu et al. 2020; Betiku et al. 2016; Betiku et al. 2018; Ohale et al. 2017; Agu et al. 2020). Mathematical expressions of the error indices (Eqs. 17–25) are tabulated in Table 2.

Process optimization

To determine the best parameters for optimum A-N removal, RSM and GA optimization techniques were adopted. To execute RSM optimization, the removal efficiency was set at maximum desirability, while the process factors were designated within the experimental constraints. For genetic algorithm (GA), a statistical exploration technique, capable of.

simulating a natural biological evolution was used in solving the optimization problems. The developed models (RSM, ANN, ANFIS) were coupled with GA and used as a decision parameter in GA optimization (which occurs through a 4-staged cycle). The cycle was sustained until the attainment of a desirable outcome; thus, the best sequence produced at the convergence of the above-described loop becomes the solution to the optimization problem (Betiku et al. 2016, 2018). RSM optimization was implemented

Table 2 The error function and adsorption mechanistic models

Error model	Mathematical expression	Eq. no
Correlation coefficient (R)	$R = \frac{\sum_{i=1}^{N}\left(y_{\text{pred.}(i)} - y_{\text{pred.}ave.}\right).\left(y_{\text{exp.}(i)} - y_{\text{exp.}ave.}\right)}{\sqrt{\left[\sum_{i=1}^{N}\left(y_{\text{pred.}(i)} - y_{\text{pred.}ave.}\right)^2\right]\left[\sum_{i=1}^{N}\left(y_{\text{exp.}(i)} - y_{\text{exp.}ave.}\right)^2\right]}}$	(17)
Coefficient of determination (R^2)	$R^2 = 1 - \frac{\sum_{i=1}^{N}\left(y_{\text{exp.}..(i)} - y_{\text{pred.}(i)}\right)^2}{\sum_{i=1}^{N}\left(y_{\text{pred.}(i)} - y_{\text{exp.}ave.}\right)^2}$	(18)
Adjusted R^2	$\text{Adjusted}R^2 = 1 - \left[\left(R^2\right)x\frac{N-1}{N-P-1}\right]$	(19)
Absolute average relative error	$\text{AARE} = \frac{1}{N}\sum_{i=1}^{N}\left(\left\lvert\frac{y_{\text{exp.}(i)} - y_{\text{pred.}(i)}}{y_{\text{exp.}(i)}}\right\rvert\right)$	(20)
Marquardt's percent standard deviation	$\text{MPSED}, \% = \sqrt{\frac{\sum_{i=1}^{N}\left[\frac{y_{\text{exp.}(i)} - y_{\text{pred.}(i)}}{y_{\text{exp.}(i)}}\right]^2}{N-P}} \times 100$	(21)
Root-mean-square error	$\text{RMSE} = \sqrt{\frac{1}{N-1}\sum_{i=1}^{N}\left(y_{\text{pred.}(i)} - y_{\text{exp.}(i)}\right)^2}$	(22)
Standard deviation	$\text{SD} = \sqrt{\frac{1}{N-1}\sum_{i=1}^{N}\left(\left\lvert\frac{y_{\text{exp.}(i)} - y_{\text{pred.}(i)}}{y_{\text{exp.}(i)}}\right\rvert - \text{AARE}\right)^2}$	(23)
Sum of squares error	$\text{SSE} = \sum_{i=1}^{N}\left(y_{\text{exp.}(i)} - y_{\text{pred.}(i)}\right)^2$	(24)
Hybrid fractional error function	$\text{HYBRID}, \% = \frac{1}{N-P}\sum_{i=1}^{N}\left[\frac{\left(y_{\text{exp.}(i)} - y_{\text{pred.}(i)}\right)^2}{y_{\text{exp.}(i)}}\right] \times 100$	(25)

using Design-Expert 11.0 trial version (Stat-Ease Inc., Minneapolis, USA), while GA optimization was carried using the optimization toolbox of MATLAB R 2015 b (Mathworks Inc.). The method of the GA algorithm is illustrated in supplementary material, Fig. S3.

Mechanistic modeling

Molecular diffusion is predictably influenced by film diffusion, pore diffusion or mass actions. However, the effect of mass action occurs rapidly; hence, it is considered negligible in the adsorption kinetics. Therefore, the liquid film adsorption mechanism is principally controlled by either film or pore diffusion (Ohale et al. 2020; Aniagor et al. 2018). To investigate the rate-limiting step in the adsorptive process of A–N onto Fe–CS, mechanistic models listed in Table 3 are applied (Ohale et al. 2020; Onu et al. 2020; Aniagor et al. 2018).

Results and discussion

AWW characterization

The AWW is typically assessed using the parameters tabulated in Table 4. From the results shown, the amount of A-N present in the raw effluent was significantly higher than the stipulated discharge limit by NESREA and WHO (Ohale et al. 2020; Onu et al. 2020). Aside from the pollutant of interest (A–N), other wastewater characterization indicators such as biochemical oxygen demand (BOD_5) and chemical oxygen demand (COD) were considerably higher than the specified discharge limit. This may be due

Table 3 The expression of the mechanistic models applied in the study

Mechanistic model	Mathematical expression	Eq. no
Webber Morris	$q_t = k_{id}t^{1/2} + C_{id}$	(26)
Double exponential	$q_t = q_e - \frac{D_1}{m_{\text{ads.}}}\exp\left(-k_{D_1}t\right) - \frac{D_2}{m_{\text{ads.}}}\exp\left(-k_{D_2}t\right)\ln\left(q_e - q_t\right) = \ln\left(\frac{D_2}{m_{\text{ads}}}\right) - k_{D_2}t$	(27)
Liquid film diffusion	$\ln(1-F) = -k_{fd}t \quad \left(F = \frac{q_t}{q_e}\right), \left(F = \frac{q_t}{q_e}\right) B_t = -\ln\left(\frac{\pi^2}{6}\right) - \ln(1 - F(t)),$	(28)
Homogeneous solid diffusion	$F = 6\left(\frac{D_s}{R^2\pi}\right)^{1/2} t^{1/2} \quad \left(F = \frac{q_t}{q_e}\right)$	(29)
Richenberg (Boyd) model	$B_t = -\ln\left(\frac{\pi^2}{6}\right) - \ln(1 - F(t)), \rightarrow F > 0.85$	(30)
	$B_t = \left(\sqrt{\pi} - \sqrt{\pi - \frac{\pi^2 F(t)}{3}}\right)^2, \rightarrow F < 0.85 \quad \left(F = \frac{q_t}{q_e}\right)$	(31)

Table 4 The physicochemical characteristics of AWW

Parameter	Raw AWW	Discharge limits		
		NESREA	FEPA	WHO
pH	7.2 ± 1.2	6 – 9	6 – 9	6.8–8.2
Turbidity (NTU)	599 ± 0.14	–	< 100	< 11.75
Biochemical oxygen demand (BOD_5), mg/L	483 ± 0.13	30	210	40
Chemical oxygen demand, mg/L	676 ± 0.23	60	< 180	250
Total organic carbon, mg/L	582 ± 0.18	–	–	–
Total phosphorus, mg/L	77.6 ± 0.08	3.5	–	5.0
Total suspended solids, mg/L	1030.8 ± 0.64	25	< 100	< 50
Total solids, mg/L	2814.8 ± 0.16	1000	< 2000	500
Total dissolved solids, mg/L	1784 ± 0.19	500	–	< 500
Ammonia Nitrogen, mg/L	103 ± 0.63	15	–	10
Nitrate, mg/L	11.97 ± 0.26	–	–	–
Potassium, mg/L	21.2 ± 0.02	–	–	–
Color, Pt scale (mg/L)	302.1 ± 0.16	–	–	–
Odor	Objectionable	Odorless	Odorless	Odorless

to the presence of substantial amounts of organic matter in AWW (Okey-Onyesolu et al. 2020). The recorded pH values ranged between pH 7.0 and pH 7.4, the values which are well within the tolerable NESREA, WHO and FEPA discharge limits (Okey-Onyesolu et al. 2020; Onu et al. 2020). The high A–N content of our AWW sample justifies the need for predisposal treatment.

Characterization of CS, Fe–CS and Fe–CS loaded A–N

FTIR analyses

FTIR is a dynamic technique that provides valuable information regarding the surface chemistry of substances. Depicted in Fig. 2a are the FTIR spectra of CS, Fe–CS and Fe–CS-loaded A–N. The FTIR spectrum of CS indicated the presence of important peaks at wave-numbers 3324.8, 2903.6,

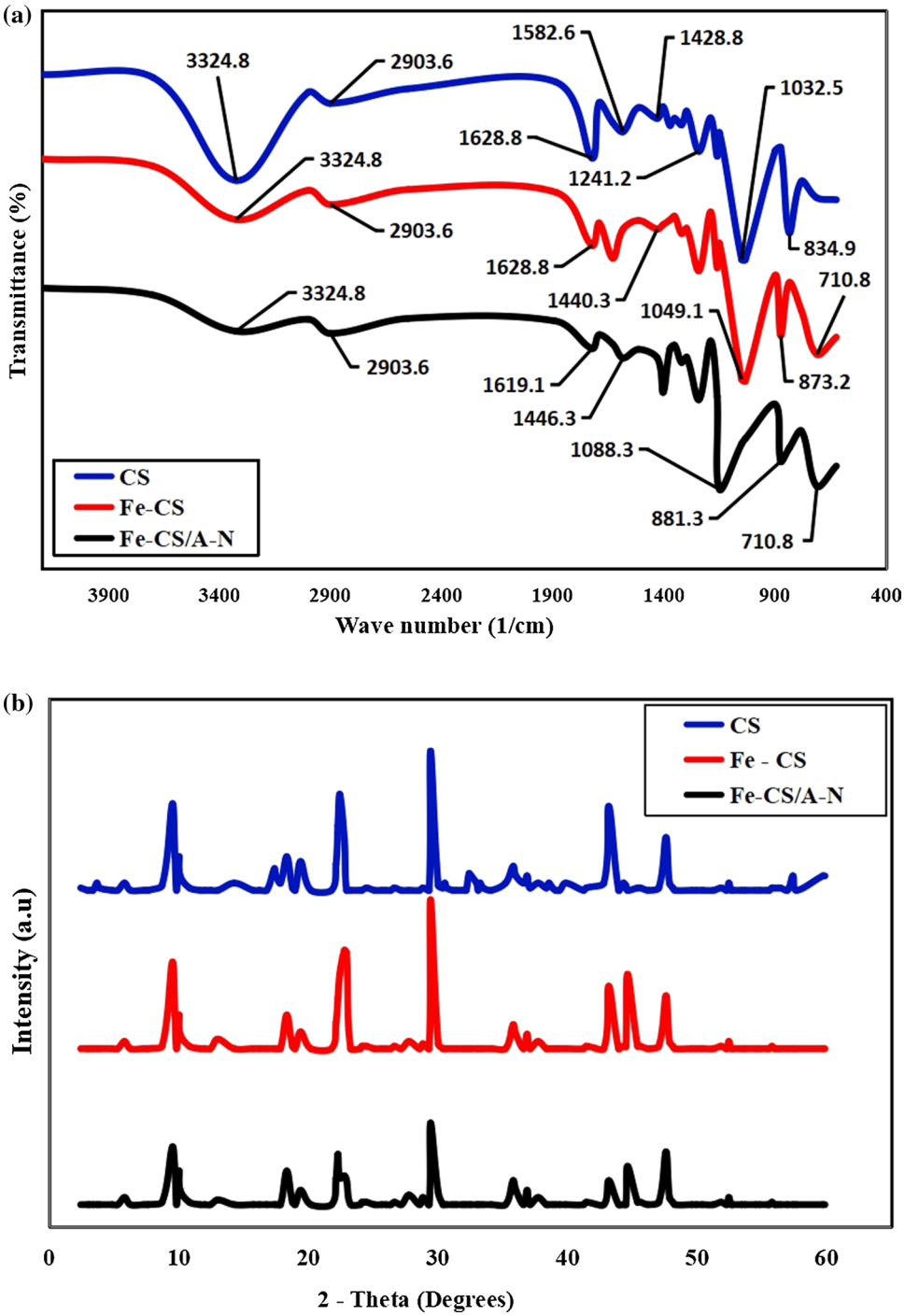

Fig. 2 **a** FTIR spectra and **b** XRD pattern

1628.8, 1582.6, 1428.8, 1241.2, 1032.5, and 834.9 cm^{-1}. The waveband at 3324.8 cm^{-1} is attributed to the presence of an aromatic group, while the strong absorption peak at 1032.5 cm^{-1} demonstrates the presence of an aliphatic C-H stretching group. The existence of amide—I (C = O secondary amide stretch) and amide—II (C-N stretch, N–H bend) in the CS were represented by waveband at 1628.8 and 1582.6 cm^{-1}, respectively, while those at 2903.6 cm^{-1} denotes the presence of amide C-H stretching. The presence of phosphorus compound of P-F stretching and methyl group with C-N bending was illustrated by adsorption band at 834.9 cm^{-1} and 1428.8 cm^{-1}, respectively. A similar observation was reported by Ohale et al. (2020).

The post-functionalization FTIR spectrum of Fe-CS displayed several recognizable peaks. The bands at 3324.8, 2903.6 and 1628.8 cm^{-1}, associated with aromatic and amide groups of CS were retained, although with diminished intensities. Slight deviations in the 1032.5–1049.1 cm^{-1} wave-numbers are assigned to the -OH deformation vibration due to the Fe-CS thermal activation. The appearance of a new peak at 710.8 cm^{-1}, in addition to the observed alterations in some others (for instance, the wave-numbers at 1428.8 and 834.9 cm^{-1} shifted to 1440.3 and 873 cm^{-1}, respectively), reveals characteristic calcite spectra (Ohale et al. 2020; Dai et al. 2017).

The post-adsorption FTIR spectrum of Fe–CS-loaded A–N showed obvious wave-number shifts. The C = O amide stretch previously domicile at 1628.8 shifted to 1619.1 cm^{-1}, with a corresponding intensity reduction. The sharp peak at 1049.1 cm^{-1} further shifted to 1088.3 cm^{-1}, while the band at 873.2 cm^{-1} slightly deviated to 881.3 cm^{-1}. These vibrational deviations and intensity reduction, especially as it relates to the amide functional groups, suggest their significant contributions during the A-N adsorptive uptake.

XRD analyses

The crystallographic features of CS, Fe–CS, and Fe–CS-loaded A–N determined via XRD technique are depicted in Fig. 2b. The XRD pattern of CS portrays a well-structured spectral pattern with prominent 2-theta reflections at 9.5°, 22.9°, 29.4°, 43.2°, and 47.6°. The XRD pattern of Fe–CS exhibited similar 2-theta reflections as CS; however, stronger peaks were observed for Fe–CS at 22.9° and 29.4°. The pronounced peaks at 22.9°, 29.4°, and 43.2° indicate that the principal crystal in CS and Fe–CS was calcite. Meanwhile, the higher 2-theta reflection intensity at 29.4° in Fe–CS illustrated a significant concentration of calcite crystal in Fe–CS compared to CS. The presence of ferric-based crystal in Fe–CS was illustrated by the 2-theta reflection at 44.6°. This observation is just as expected because iron nitrate was utilized during the CS functionalization process. Similar observations have been reported elsewhere (Ohale et al. 2020; Dai et al. 2017). The post-adsorption XRD pattern indicated minor alterations in the Fe–CS-loaded A–N structural configuration, thus, illustrating the crystalline stability of Fe–CS despite the A–N adsorption.

SEM analyses

SEM analyses fundamentally examine the particle size, porosity, and morphological properties of any given adsorbents. The surface morphology of CS (Fig. 3a) depicts the existence of a layer-stacking structure with irregular flakes, an indication that the CS was composed of fibrillary structure and crispy rough edges (Ohale et al. 2020). Figure 3b (SEM image of Fe–CS) shows the development of superior surface cohesion, with moderate thin layer tissues and a coral-like porous structure. These improvements in the surface properties of Fe–CS are attributed to the modification techniques carried out during the CS functionalization procedure. The morphological micrograph of Fe–CS-loaded A–N as depicted in Fig. 3c shows the appearance of an intense river-like morphology, thus, validating effective adsorption of A–N onto Fe–CS.

TGA analyses

TGA was conducted to evaluate the mass stability of CS with temperature variations. The TGA results serve as a useful guide for the selection of suitable thermal activation temperatures (Ohale et al. 2020; Sebestyén et al. 2020). TGA result of CS, Fe–CS, and Fe–CS-loaded A–N is illustrated in Fig. 3d, and the respective curves portrayed three (3) thermal process stages. For CS, the first stage was recorded between 50 and 195 °C. During this period, a 6% loss of initial mass was recorded, a development which could be attributed to the volatilization of surface organic matter and water desorption. The second stage, which illustrates an accelerated mass reduction, was observed between 225 and 330 °C. This stage accounted for a 38% loss of CS mass. This massive weight loss is unconnected with the probable dehydroxylation of the OH functional group and decomposition of the acetyl groups (Ren et al. 2021). Beyond 330 °C, CS attained the final stage of thermal equilibrium, which was sustained until its termination at 600 °C.

Fe–CS and Fe–CS loaded A–N exhibited very similar thermal behavior as demonstrated in Fig. 3d. The initial stage for both samples (Fe–CS and Fe–CS-loaded A–N) occurred between 50 and 350 °C. This characteristic of high thermal stability was a direct consequence of the Fe–CS calcination step. Between 350 and 370 °C, a rapid mass loss which accounted for about 19.5 and 25% weight reduction in Fe–CS and Fe–CS loaded A–N, respectively, was recorded. However, the samples (Fe–CS and Fe–CS-loaded A–N) attained thermal equilibrium beyond 370 °C. The TGA result

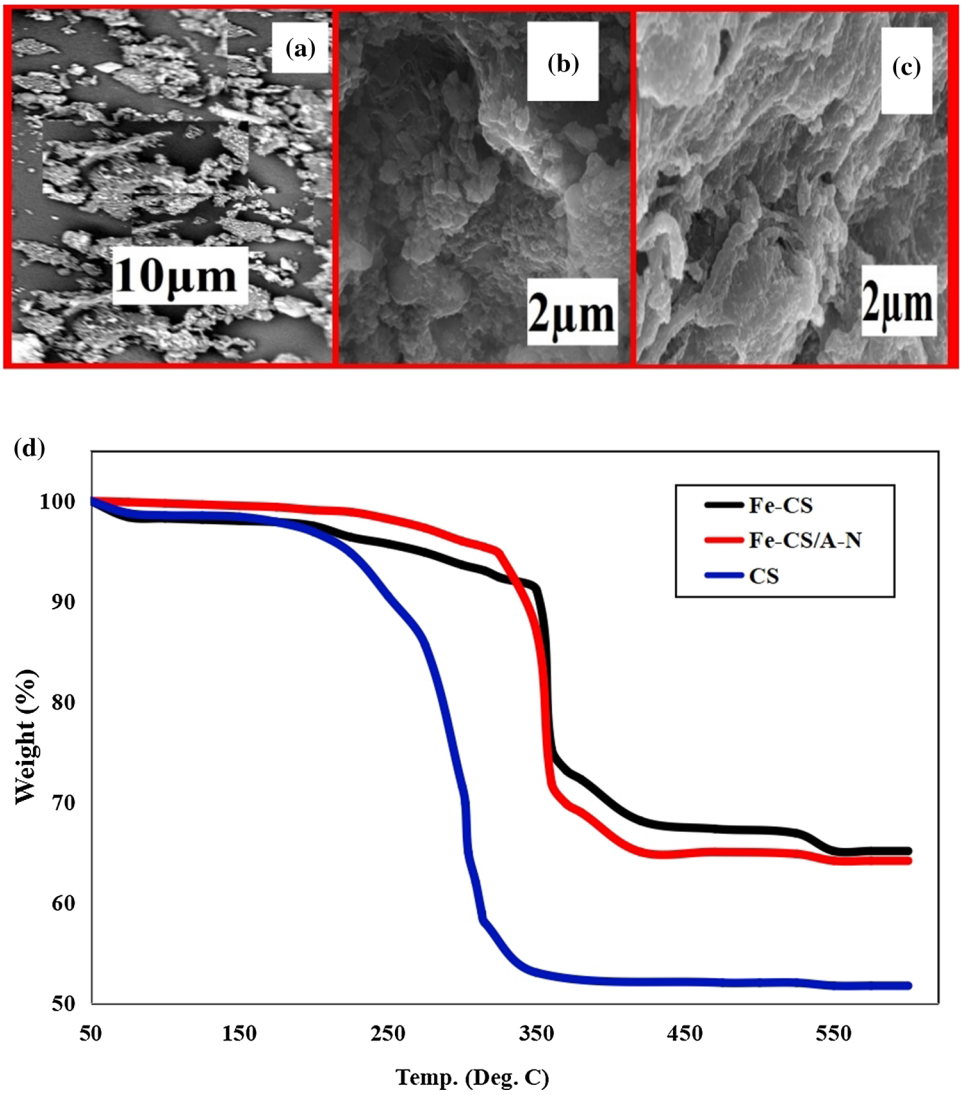

Fig. 3 SEM micrograph for **a** CS **b** Fe–CS **c** Fe–CS-loaded A–N and **d** TGA analyses spectra

further showed that Fe–CS is more thermally stable than Fe–CS-loaded A–N. Such observation is not surprising, noting that Fe–CS-loaded A–N contained a substantial amount of imbibed adsorbate, which contributed significantly to its weight.

Experimental design

RSM

The combined effects of pH, Fe–CS dosage, initial concentration, temperature, and contact time on the A–N removal efficiency were studied using a central composite design. Results obtained from the respective experimental runs are presented with supplementary material (Table S1). Table 5 shows the relevant parameters generated from the analysis of variance (ANOVA). The ANOVA technique employs p value and f-value to determine the adequacy and fit goodness of the empirical models. A confidence level of 95% was used to analyze the probability of p value; thus, the lower the p values (p values < 0.05), the higher the significance of the corresponding model term and vice versa (Onu et al. 2021b). The full quadratic model and the reduced quadratic model obtained after the elimination of the insignificant terms are presented in Table 5**.** Meanwhile, the developed RSM model prediction is given in Eq. (32).

Besides the p values, the f-values are also useful in ascertaining the significance of each term in the quadratic model. This was accomplished by evaluating the ratio between the mean square and the residual error of the quadratic model. Hence, by comparing the models' lack of fit parameters for the reduced quadratic model, an f-value of 107.96 (Table 5) was recorded, an implication that the quadratic model is significant, relative to the pure error. The lack of fit f-value of 1.09 also implies the lack of fit is not significant relative to the pure error. Lack of fit p-value suggests that there is a

Table 5 Test of significance for model coefficients and analysis of variance

Full quadratic model			Reduced quadratic model							
source	sum of squares	D*f*	mean squares	*f*-value	*P* value	sum of squares	d*f*	mean squares	*f*-value	*p* value
x_1	341.0	1	341.0	33.7	0.0001	341.0	1	341.0	33.4	< 0.0001
x_2	2899.2	1	2899.2	286.0	< 0.0001	2899.2	1	2899.2	284.5	< 0.0001
x_3	2328.4	1	2328.4	229.8	< 0.0001	2328.4	1	2328.4	228.5	< 0.0001
x_4	2558.1	1	2558.1	252.4	< 0.0001	2558.1	1	2558.1	251.0	< 0.0001
x_5	382.6	1	382.6	37.8	< 0.0001	382.6	1	382.6	37.6	< 0.0001
x_1x_2	24.4	1	24.4	2.4	0.1489	–	–	–	–	–
x_1x_3	327.8	1	327.8	32.4	< 0.0001	327.8	1	327.8	32.1	< 0.0001
x_1x_4	0.56	1	0.56	0.06	0.819	–	–	–	–	–
x_1x_5	81.0	1	81.0	7.9	0.0164	81.0	1	81.0	7.9	0.0129
x_2x_3	448.6	1	448.6	44.3	< 0.0001	448.6	1	448.5	44.0	< 0.0001
x_2x_4	386.1	1	386.1	38.1	< 0.0001	386.1	1	386.0	37.8	< 0.0001
x_2x_5	790.4	1	790.4	78	< 0.0001	790.4	1	790.4	77.6	< 0.0001
x_3x_4	284.1	1	284.1	28.0	0.0003	284.1	1	284.1	27.9	< 0.0001
x_3x_5	55.6	1	55.6	5.5	0.03900	55.6	1	55.6	5.4	0.0337
x_4x_5	5.5	1	5.5	0.55	0.4757	–	–	–	–	–
x_1^2	2217.7	1	2217.7	218.8	< 0.0001	2299.7	1	2299.7	225.7	< 0.0001
x_2^2	383.8	1	383.8	37.8	< 0.0001	408.5	1	408.4	40.0	< 0.0001
x_3^2	753.1	1	753.1	74.3	< 0.0001	791.3	1	791.2	77.6	< 0.0001
x_4^2	382.7	1	382.7	37.7	< 0.0001	407.2	1	407.2	39.9	< 0.0001
x_5^2	10.8	1	10.8	1.07	0.3222	–	–	–	–	–
ANOVA										
Model	17,644.0	20	882.2	87.06	< 0.0001	17,602.6	16	1100.1	107.9	< 0.0001
Lack of fit	63.32	6	10.55	1.1	0.4699	104.7	10	10.5	1.09	0.4935
Residual	111.47	11	10.13			152.8	15	10.2		
Pure error	48.15	5	9.63			48.1	5	9.6		
Adequacy precision = 34.38						Adequacy precision = 40.789				
C. V. (%) = 3.05						C. V. (%) = 3.07				
Mean = 35.18						Mean = 35.18				

49.35% chance that the f-value for lack of fit is attributable to noise. Furthermore, the predicted R–squared of 0.9507 is in reasonable agreement with the adjusted *R*–squared ($R^2 = 0.9822$), thus, suggesting the reproducibility of the RSM model (Ohale et al. 2017; Onu et al. 2020, 2021a; Betiku et al. 2018). The adequacy of the quadratic model is evaluated using the normal plot of residuals shown in Fig. 4a**.** It was observed that the residuals sustain a close alignment with the normality line, thereby, confirming the normality of the residual points.

Conversely, the plot of residuals vs. predicted values shown in Fig. 4b illustrates the random positioning of residuals around the baseline. This observation is a further indication of the suitability and accuracy of the developed quadratic model. An indication for the signal-to-noise ratio is given by the adequate precision value (APR). According to Betiku et al. (2018), for a model to effectively navigate the design space, an APR greater than 4.0 is required. Therefore, an APR of 40.789 recorded in this study (Table 5) indicates the occurrence of sufficient signals relative to the noise. Also, the obtained coefficient of variance (CV) value (3.07%) indicates that the quadratic model was satisfactorily reproducible, judging from the assertions made by Onu et al. (2021a). The effect of the respective model term on the overall removal efficiency prediction was demonstrated using the Pareto effect plot (Fig. 4c), while the influence of the corresponding factors was estimated using Eq. (33). Figure 4c shows that the Fe–CS dosage (x_2) sustained the greatest influence on the A–N removal efficiency, thus buttressing its (Fe-CS) adsorptive applicability.

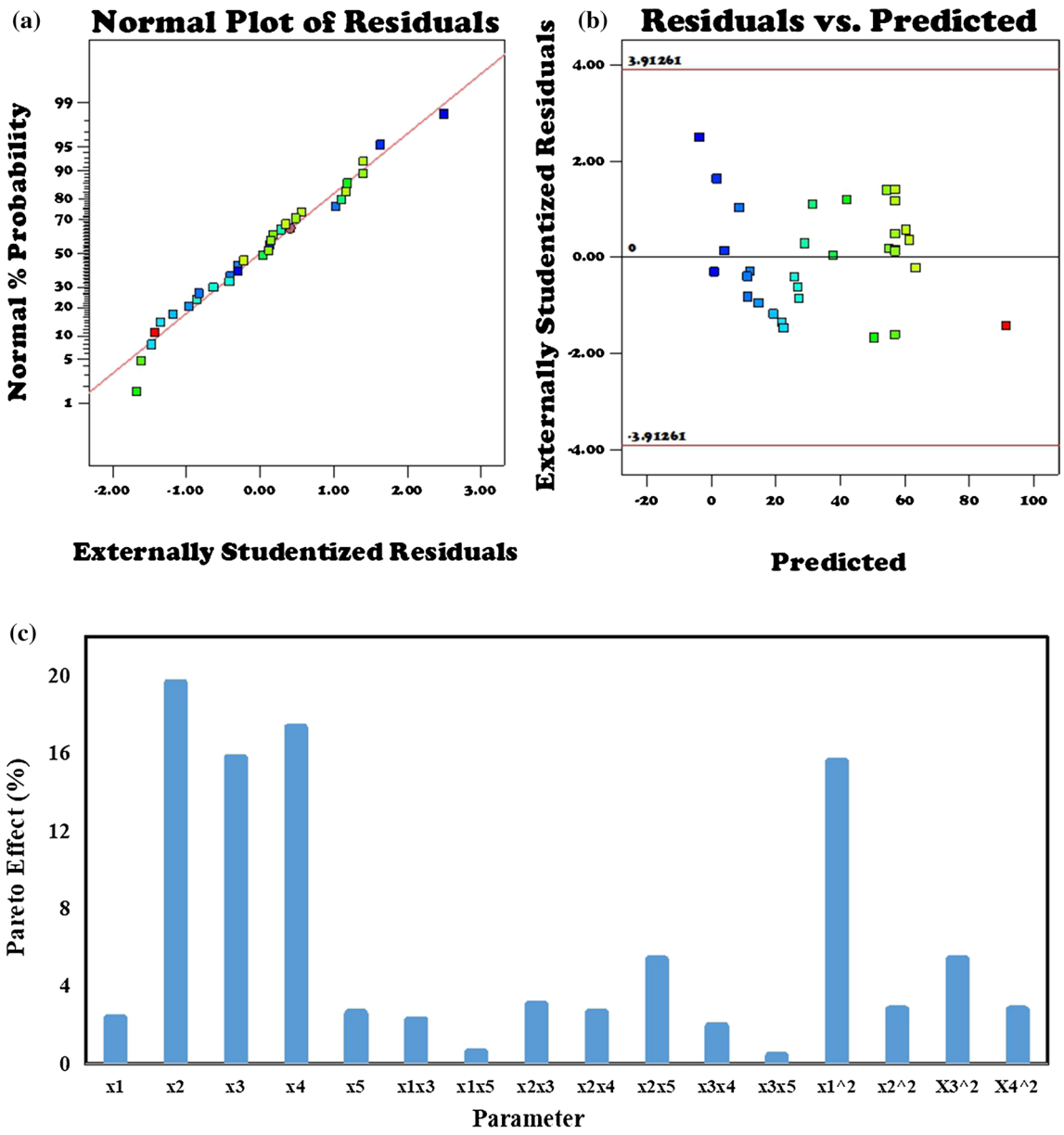

Fig. 4 RSM plots for **a** Normal residuals, **b** residual vs. predicted, and **c** Pareto effect

$$\begin{aligned} A-N \text{ rem. } (\%) = {} & 45.7989x_1 - 449.7647x_2 + 9.5928x_3 + 148.8144x_4 \\ & - 0.1576x_5 + 0.0794x_1x_3 - 0.0187x_1x_5 - 0.3096x_2x_3 \\ & + 1.6374x_2x_4 + 0.1952x_2x_5 - 0.0296x_3x_4 - 3.5087\,x_1^2 \\ & - 16.4300x_2^2 - 0.0101x_3^2 - 0.2362x_4^2 - 23591.2578 \end{aligned} \tag{32}$$

$$P_i = \left[\frac{b_i}{\sum b_i}\right] x100 \tag{33}$$

where b is the f-value for the respective model term.

ANN

The graphical expression for the topological analysis of ANN is presented in Fig. 5(a–d) the data partitioning (as a training set and test set) was conducted to eliminate over-training and over parameterization (Ohale et al. 2017; Onu

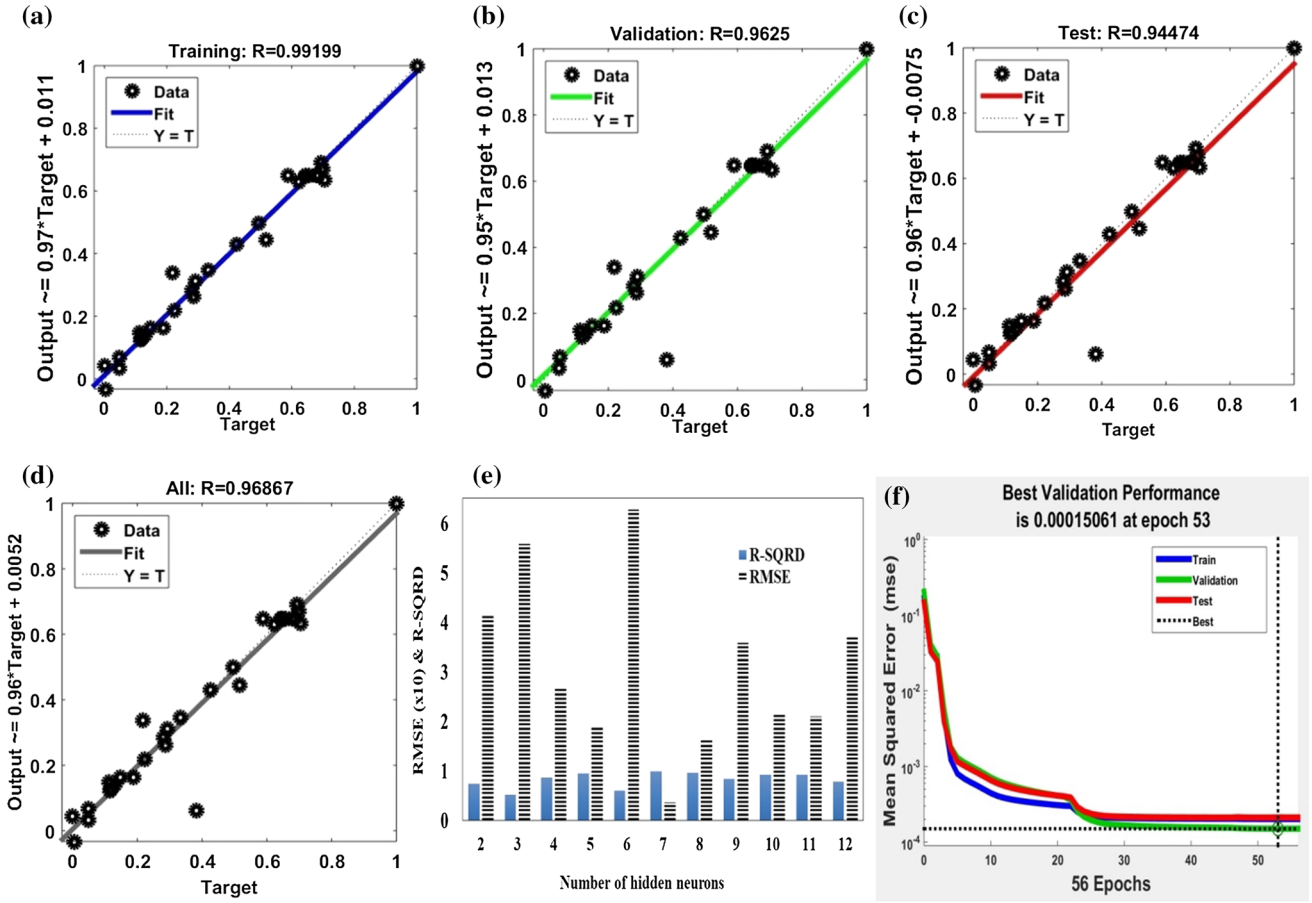

Fig. 5 ANN plots for **a** training data **b** validation data **c** test data **d** overall data **e** effect of hidden neurons and **f** performance evaluation

et al. 2021b). Based on the hidden neurons selection criteria described in "ANN" Section, seven hidden neurons emerged as the most appropriate, because they depicted the least root-mean-square error (RMSE = 0.3619) and highest correlation coefficient ($R^2 = 0.9981$) values (see Fig. 5e). Hence, the developed network was described as a 5–7–1 (five input neurons, seven hidden neurons, and one output neuron) ANN architecture. Furthermore, the correlation coefficients obtained from the regression plots were 0.9919, 0.9625, 0.9447, and 0.9686 for training, validation, testing, and overall data sets, respectively, evidence for a high correlation between experimental data and ANN predictions. The consistency of the training process was estimated using the validation performance plot shown in Fig. 5f. The best validation performance of the training network generated a mean square error of 1.5061E-04 at the 53rd epoch iteration. The negligible mean square error value recorded for the study suggests that the absence of any over-fitting difficulty within the network (Onu et al. 2021a; Nwadike et al. 2020). The estimated R^2 and adjusted R^2 of the ANN model were 0.9025 and 0.8945, respectively. This suggests that 90.25% of the variations in experimental and predicted values can be described by the ANN model. Significant R^2 value established for the ANN model illustrates its capability in capturing the nonlinear nature of the adsorptive process of A–N onto Fe–CS.

Table 6 ANFIS architecture and training parameters

Number of nodes	524
Number of linear parameters	243
Number of nonlinear parameters	30
Total number of parameters	273
Number of training data set	120
Number of checking data set	55
Average training error	0.0000138
Number of testing data set	60
Average testing error	0.0000101
Number of epochs	43
Membership function	Gaussmf
Output membership function	Constant
Method of optimization	Hybrid

ANFIS

The Sugeno type ANFIS structure for five input parameters and one output variable generated by grid partitioning is displayed in Fig. S1 (Supplementary data). The ANFIS structure was designed using a hybrid learning procedure that incorporates the least square and gradient technique. To enhance the effectiveness of the system, the raw data were normalized using Eq. (5). Among the five tested membership functions (trimf, trapmf, gbellmf, gaussmf, and guass2mf), gaussmf was selected as the most suitable for the development of the fuzzy inference system (FIS). The ANFIS architecture and training parameters are listed in Table 6.

Plots of the experimental and predicted A–N removal rates against run numbers for training, testing, checking, and overall data set are illustrated in Fig. 6(a–d), respectively. The significant spread of the interwoven data depicted in these plots is indicative of a high correlation between experimental and ANFIS predicted data. Furthermore, the calculated values R^2 and adjusted R^2 of the overall model performance were 0.9998 and 0.9978, respectively. This high R^2 further gave credence to the ability of the ANFIS model in predicting the A–N adsorptive removal (Onu et al. 2021a). The adjusted R^2 value implies that the ANFIS model can describe 99.78% of the variability between the experimental and predicted values (Betiku et al. 2018).

Table 7 Statistical appraisal of RSM, ANN and ANFIS

Parameter	RSM	ANN	ANFIS
R	0.9898	0.9500	0.9999
R^2	0.9799	0.9025	0.9998
Adj-R^2	0.9761	0.8845	0.9978
AARE	3.0847	4.3016	0.0075
MPSED (%)	23.2849	27.0725	0.0307
RMSE	16.9717	19.7323	0.0224
SD	16.9560	19.5659	0.0214
SSE	108.0657	1368.0471	48.2191
HYBRID (%)	3.5639	16.7914	0.0324

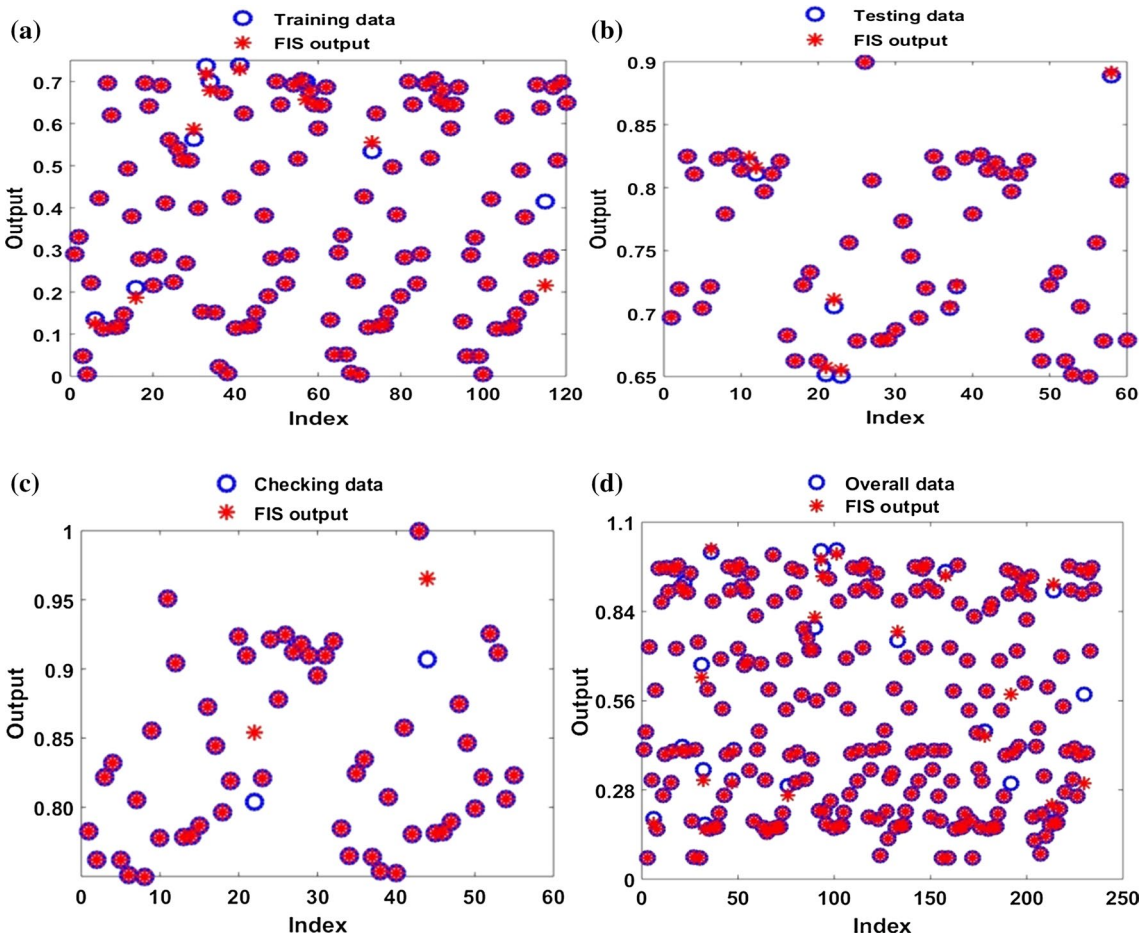

Fig. 6 ANFIS plots for **a** training data, **b** testing data, **c** checking data, and **d** overall data

Model appraisal analysis

The precision of established models (RSM, ANN, and ANFIS) in estimating the A–N removal was appraised by comparing their error variance using the models presented in Table 2 and the results are presented in Table 7**.** According to Betiku et al. (2018), the value of R should be greater than 0.8 for an effective correlation between experimental and predicted values. Hence, the high R values ($R > 0.95$) obtained for the three models indicate their significant applicability in predicting experimental values. Adjusted R^2 is applied for testing the extent of R^2 overestimation, and its values obtained for the three models were satisfactorily sufficient, thus, validating their importance in predicting the A–N adsorptive removal. AARE was used to estimate the mean relative error between the model predictions and experimental values. However, the ANFIS model yielded negligible AARE values, a demonstration of its (ANFIS model) prediction accuracy and superiority over RSM and ANN. MPSED estimates the geometric error distribution of a system and allows for several degrees of freedom. The values of MPSED obtained for RSM, ANN, and ANFIS were 23.3%, 27.1%, and 0.03%, respectively, which demonstrates the high prediction accuracy of the ANFIS model in capturing the nonlinear nature of the adsorptive process. Low error magnitudes obtained by testing other statistical indicators (RMSE, SSE, SD, HYBRID) on the outputs (Table 7) further gave credence to the superiority of the ANFIS model in the data prediction accuracy of the present study.

In general, results obtained from statistical analysis indicate that ANFIS was the most effective model, while ANN was the least effective model in predicting the adsorptive removal of A–N from AWW onto Fe–CS. Thus, the prediction accuracy of the studied models followed the order: ANFIS > RSM > ANN. The results obtained here correlate favorably with the findings of Onu et al. (2020) and Dastorani et al. (2010).

Effect of process variables

Figure 7a and b presents the contour plots for the temperature-dosage, and temperature-concentration effects, respectively. Both figures illustrate the positive impact of temperature on the removal efficiency and the entire adsorptive process. At all levels of adsorbent dosage and effluent concentration, an increase in the system temperature resulted in a rapid removal rate, as depicted in the 2D contour plots of Fig. 7(a–d). Onu et al. (2021a, b), had earlier reported the augmentation of the adsorbate–adsorbent interaction rate and strengthening of the adsorbate ions' mobility due to temperature increase. This phenomenon explains the observed increase in the removal efficiency upon temperature increase; thus, an endothermic process. Figure 7(b–e) depicts the 3D surface plots for the pH-dosage, and pH-concentration effects, respectively. The figures demonstrated that pH has a prominent quadratic effect on the A–N removal. At any given adsorbent dosage, increasing the pH from 4.0 to 6.8 resulted in a rapid A–N removal rate. However, increasing pH beyond pH 6.8 decreased the A–N removal efficiency (see Fig. 7b and e). Under slightly acidic conditions (pH 4.0–6.8), high amounts of H + competes with the ionized ammonia (NH_4^+) for available adsorption sites on Fe–CS, thus resulting in a reduced.

removal rate. Similarly, from Eq. (34), it is evident that a large amount of NH_4^+ was converted to $NH_3.H_2O$ molecule in an alkaline medium. The production of non-ionized $NH_3.H_2O$ resulted in adsorption difficulties and reduced removal rate of A–N in alkaline medium.

$$NH_4^+ + OH^- \rightarrow NH_3.H_2O \tag{34}$$

The effect of initial concentration on the removal efficiency was studied via a variation in the A–N initial concentration from 1.75 to 87.25 mg/L (see supplementary material, Table S1). Figure 7(c–e) shows a continuous reduction in A–N removal efficiency due to a progressive increase in initial concentration. This trend is attributed to the increased occupation of readily available adsorption sites on the surface of Fe–CS. Conversely, the effect of Fe–CS dosage depicted a reverse trend (Fig. 7f), as more active sites were made available upon the Fe–CS dosage increase from 1.0–2.2 g. This increment subsequently enhanced the A-N removal efficiency, as demonstrated in Fig. 7f. Similar observations have been reported by other researchers (Ohale et al. 2020; Aniagor et al. 2018; Onu et al. 2021a, b; Okafor et al. 2015).

Process optimization

Four optimization techniques (RSM-GA, ANFIS-GA, ANN-GA, and RSM) were applied for optimizing the selected input variables (pH, dosage, concentration, temperature, and time) used for modeling the adsorptive process. The optimization is aimed at maximizing the A–N removal efficiency. The range of constraints used for genetic algorithm optimization is given in Eq. (35)–Eq. (39), while optimum values for A–N removal efficiency predicted by each method are given in Table 8**.** The graphical solutions for the RSM-GA, ANFIS-GA and ANN-GA optimization processes are given in Fig. 8(a–c), respectively. Judging by the figures, the removal efficiency increased steadily in a stepwise order from generation G_1–G_{198} for RSM-GA; generation G_1–G_{110} for ANFIS-GA; and generation G_1–G_{182} for ANN-GA, and subsequently remained constant until termination of the process. Such observations suggest the absence of a probable crossover or mutation, with

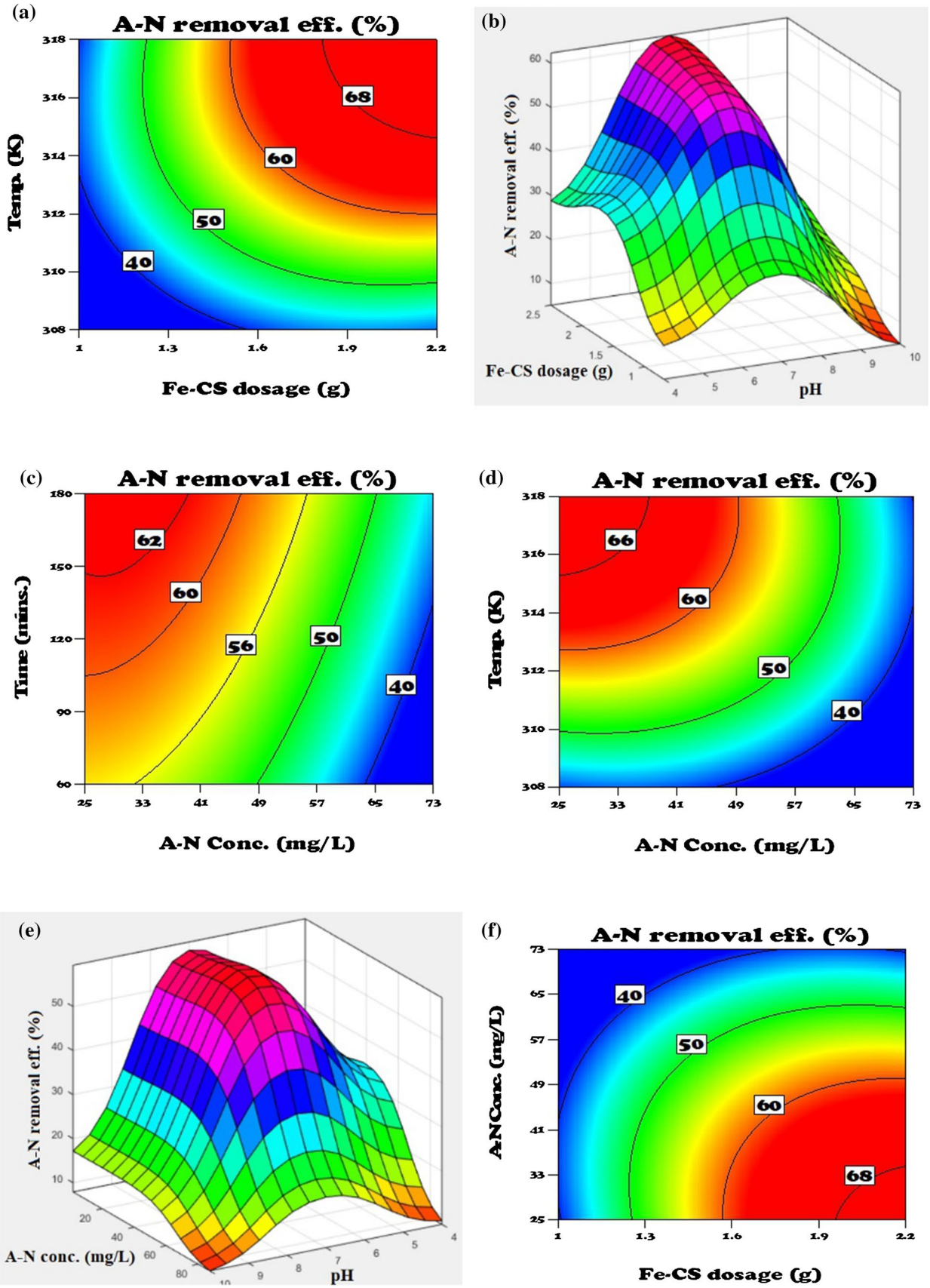

Fig. 7 Surface and contour plots for the adsorption of A–N adsorption onto Fe–CS

Table 8 Optimization and model validation parameters

Tool	x_1 pH	x_2 dosage (g)	x_3 conc (mg/L)	x_4 Temp (K)	x_5 Time (min)	Rem. Eff. (%)	
						Predicted	Actual
RSM-GA	6.7	2.20	22.4	316	165	92.00	89.82
ANN-GA	6.2	2.19	17.1	318	168	91.58	89.01
ANFIS-GA	6.5	2.18	18.8	317	156	92.60	90.06
RSM	6.3	2.17	19.18	317	163	91.80	88.25

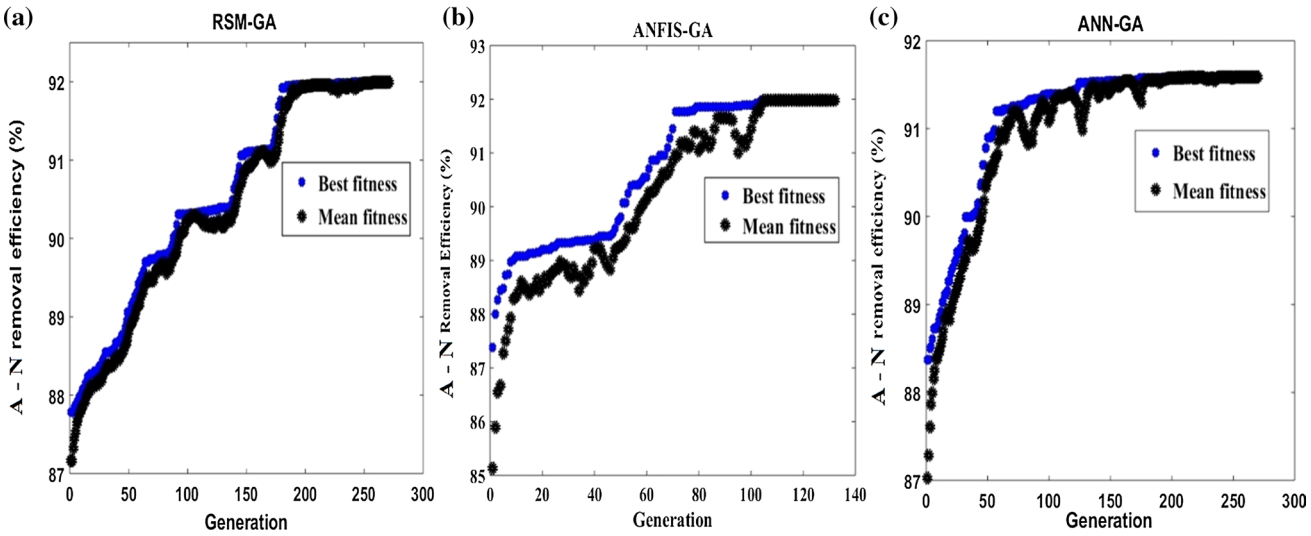

Fig. 8 Genetic algorithm optimization for **a** RSM-GA **b** ANFIS-GA and **c** ANN-GA

a substantive optimization effect within the parameters (Betiku et al. 2018, 2016).

Duplicate validation experiments were conducted at the predicted optimum conditions, and the average A–N removal efficiency was calculated and is recorded as actual removal efficiency in Table 8. ANFIS-GA gave the highest A–N removal efficiency prediction of 92.60% (at pH 6.5, 2.2 g, 18.8 mg/L, 317 K, and 156 min). The superiority of ANFIS-GA prediction performance over those of RSM-GA and ANN-GA is linked to their experimental data capturing accuracy. Therefore, regarding the quality and accuracy of the optimized process variables, the observed performance of the optimization techniques followed the trend: ANFIS-GA > RSM-GA > ANN-GA > RSM.

$$5.0 \leq \text{pH} \leq 9.0 \tag{35}$$

$$1.0(g) \leq \text{Fe} - \text{CSdosage} \leq 2.2(g) \tag{36}$$

$$16\left(\frac{\text{mg}}{L}\right) \leq A - N\text{concentration} \leq 73\left(\frac{\text{mg}}{L}\right) \tag{37}$$

$$308(K) \leq \text{Temperature} \leq 318(K) \tag{38}$$

$$60(\text{min}.) \leq \text{time} \leq 180(\text{min}.) \tag{39}$$

Mechanistic modeling

The adsorption kinetic data interpretation from a mechanistic viewpoint is an important step in describing the sorption process, and the accurate identification of the predominant sorption mechanism is also paramount for design purposes (Ohale et al. 2020). Generally, for an adsorption system, the solute transfer mechanism is typically characterized by either boundary layer diffusion (film) or intraparticle diffusion (pore), or both. Meanwhile, the final adsorption stages are mostly regarded as the equilibrium step, provided the adsorptive.

simulating a natural biological evolution was used in solving the optimization problems. The developed models (RSM, ANN, ANFIS) were coupled with GA and used as a decision parameter in GA optimization (which occurs through a 4-staged cycle). The cycle was sustained until the attainment of a desirable outcome; thus, the best sequence produced at the convergence of the above-described loop becomes the solution to the optimization problem (Betiku

et al. 2016, 2018). RSM optimization was implemented using Design-Expert 11.0 trial version (Stat-Ease Inc., Minneapolis, USA), while GA optimization was carried using the optimization toolbox of MATLAB R 2015 b (Mathworks Inc.). The method of the GA algorithm is illustrated in supplementary material, Fig. S3.

Mechanistic modeling

Molecular diffusion is predictably influenced by film diffusion, pore diffusion or mass actions. However, the effect of mass action occurs rapidly; hence, it is considered negligible in the adsorption kinetics. Therefore, the liquid film adsorption mechanism is principally controlled by either film or pore diffusion (Ohale et al. 2020; Aniagor et al. 2018). To investigate the rate-limiting step in the adsorptive process of A–N onto Fe–CS, mechanistic models listed in Table 3 are applied (Ohale et al. 2020; Onu et al. 2020; Aniagor et al. 2018).

Results and discussion

AWW characterization

The AWW is typically assessed using the parameters tabulated in Table 4. From the results shown, the amount of A-N present in the raw effluent was significantly higher than the stipulated discharge limit by NESREA and WHO (Ohale et al. 2020; Onu et al. 2020). Aside from the pollutant of interest (A–N), other wastewater characterization indicators such as biochemical oxygen demand (BOD_5) and chemical oxygen demand (COD) were considerably higher than the specified discharge limit. This may be due to the presence of substantial amounts of organic matter in AWW (Okey-Onyesolu et al. 2020). The recorded pH values ranged between pH 7.0 and pH 7.4, the values which are well within the tolerable NESREA, WHO and FEPA discharge limits (Okey-Onyesolu et al. 2020; Onu et al. 2020). The high A–N content of our AWW sample justifies the need for their predisposal treatment.

Characterization of CS, Fe–CS and Fe–CS-loaded A–N

FTIR analyses

FTIR is a dynamic technique that provides valuable information regarding the surface chemistry of substances. Depicted in Fig. 2a are the FTIR spectra of CS, Fe–CS and Fe–CS-loaded A–N. The FTIR spectrum of CS indicated the presence of important peaks at wave-numbers 3324.8, 2903.6, 1628.8, 1582.6, 1428.8, 1241.2, 1032.5, and 834.9 cm^{-1}. The waveband at 3324.8 cm^{-1} is attributed to the presence of an aromatic group, while the strong absorption peak at 1032.5 cm^{-1} demonstrates the presence of an aliphatic C-H stretching group. The existence of amide—I (C = O secondary amide stretch) and amide—II (C-N stretch, N–H bend) in the CS were represented by waveband at 1628.8 and 1582.6 cm^{-1}, respectively, while those at 2903.6 cm^{-1} denotes the presence of amide C-H stretching. The presence of phosphorus compound of P-F stretching and methyl group with C-N bending was illustrated by adsorption band at 834.9 and 1428.8 cm^{-1}, respectively. A similar observation was reported by Ohale et al. (2020).

The post-functionalization FTIR spectrum of Fe-CS displayed several recognizable peaks. The bands at 3324.8, 2903.6 and 1628.8 cm^{-1}, associated with aromatic and amide groups of CS were retained, although with diminished intensities. Slight deviations in the 1032.5–1049.1 cm^{-1} wave-numbers are assigned to the -OH deformation vibration due to the Fe-CS thermal activation. The appearance of a new peak at 710.8 cm^{-1}, in addition to the observed alterations in some others (for instance, the wave-numbers at 1428.8 and 834.9 cm^{-1} shifted to 1440.3 and 873 cm^{-1}, respectively), reveals characteristic calcite spectra (Ohale et al. 2020; Dai et al. 2017).

The post-adsorption FTIR spectrum of Fe–CS-loaded A–N showed obvious wave-number shifts. The C = O amide stretch previously domicile at 1628.8 shifted to 1619.1 cm^{-1}, with a corresponding intensity reduction. The sharp peak at 1049.1 cm^{-1} further shifted to 1088.3 cm^{-1}, while the band at 873.2 cm^{-1} slightly deviated to 881.3 cm^{-1}. These vibrational deviations and intensity reduction, especially as it relates to the amide functional groups, suggest their significant contributions during the A-N adsorptive uptake from AWW.

XRD analyses

The crystallographic features of CS, Fe–CS, and Fe–CS-loaded A–N determined via XRD technique are depicted in Fig. 2b. The XRD pattern of CS portrays a well-structured spectral pattern with prominent 2-theta reflections at 9.5°, 22.9°, 29.4°, 43.2°, and 47.6°. The XRD pattern of Fe–CS exhibited similar 2-theta reflections as CS, however, stronger peaks were observed for Fe–CS at 22.9° and 29.4°. The pronounced peaks at 22.9°, 29.4°, and 43.2° indicate that the principal crystal in CS and Fe–CS was calcite. Meanwhile, the higher 2-theta reflection intensity at 29.4° in Fe–CS illustrated a significant concentration of calcite crystal in Fe–CS compared to CS. The presence of ferric-based crystal in Fe–CS was illustrated by the 2-theta reflection at 44.6°. This observation is just as expected because iron nitrate was utilized during the CS functionalization process. Similar observations have been reported elsewhere (Ohale et al.

2020; Dai et al. 2017). The post-adsorption XRD pattern indicated minor alterations in the Fe–CS-loaded A–N structural configuration, thus, illustrating the crystalline stability of Fe–CS despite the A–N adsorption.

SEM analyses

SEM analyses fundamentally examine the particle size, porosity, and morphological properties of any given adsorbents. The surface morphology of CS (Fig. 3a) depicts the existence of a layer-stacking structure with irregular flakes, an indication that the CS was composed of fibrillary structure and crispy rough edges (Ohale et al. 2020). Figure 3b (SEM image of Fe–CS) shows the development of superior surface cohesion, with moderate thin layer tissues and a coral-like porous structure. These improvements in the surface properties of Fe–CS are attributed to the modification techniques carried out during the CS functionalization procedure. The morphological micrograph of Fe–CS-loaded A–N as depicted in Fig. 3c shows the appearance of an intense river-like morphology, thus, validating effective adsorption of A–N onto Fe–CS.

TGA analyses

TGA was conducted to evaluate the mass stability of CS with temperature variations. The TGA results serve as a useful guide for the selection of suitable thermal activation temperatures (Ohale et al. 2020; Sebestyén et al. 2020). TGA result of CS, Fe–CS, and Fe–CS-loaded A–N is illustrated in Fig. 3d, and the respective curves portrayed three (3) thermal process stages. For CS, the first stage was recorded between 50 and 195 °C. During this period, a 6% loss of initial mass was recorded, a development which could be attributed to the volatilization of surface organic matter and water desorption. The second stage, which illustrates an accelerated mass reduction, was observed between 225 and 330 ^{0}C. This stage accounted for a 38% loss of CS mass. This massive weight loss is unconnected with the probable dehydroxylation of the OH functional group and decomposition of the acetyl groups (Ren et al. 2021). Beyond 330 °C, CS attained the final stage of thermal equilibrium, which was sustained until its termination at 600 °C.

Fe–CS and Fe–CS loaded A–N exhibited very similar thermal behavior as demonstrated in Fig. 3d. The initial stage for both samples (Fe–CS and Fe–CS-loaded A–N) occurred between 50 and 350 °C. This characteristic high thermal stability was a direct consequence of the Fe–CS calcination step. Between 350 and 370 °C, a rapid mass loss which accounted for about 19.5% and 25% weight reduction in Fe–CS and Fe–CS loaded A–N, respectively, was recorded. However, the samples (Fe–CS and Fe–CS-loaded A–N) attained thermal equilibrium beyond 370 °C. The TGA result further showed that Fe–CS is more thermally stable than Fe–CS-loaded A–N. Such observation is not surprising, noting that Fe–CS-loaded A–N contained a substantial amount of imbibed adsorbate, which contributed significantly to its weight.

Experimental design

RSM

The combined effects of pH, Fe–CS dosage, initial concentration, temperature, and contact time on the A–N removal efficiency were studied using a central composite design. Results obtained from the respective experimental runs are presented with supplementary material (Table S1). Table 5 shows the relevant parameters generated from the analysis of variance (ANOVA). The ANOVA technique employs p value and f-value to determine the adequacy and fit goodness of the empirical models. A confidence level of 95% was used to analyze the probability of p value; thus, the lower the p values (p values < 0.05), the higher the significance of the corresponding model term and vice versa (Onu et al. 2021b). The full quadratic model and the reduced quadratic model obtained after the elimination of the insignificant terms are presented in Table 5. Meanwhile, the developed RSM model prediction is given in Eq. (32).

Besides the p values, the f-values are also useful in ascertaining the significance of each term in the quadratic model. This was accomplished by evaluating the ratio between the mean square and the residual error of the quadratic model. Hence, by comparing the models' lack of fit parameters for the reduced quadratic model, an f-value of 107.96 (Table 5) was recorded, an implication that the quadratic model is significant, relative to the pure error. The lack of fit f-value of 1.09 also implies the lack of fit is not significant relative to the pure error. Lack of fit p-value suggests that there is a 49.35% chance that the f-value for lack of fit is attributable to noise. Furthermore, the predicted R–squared of 0.9507 is in reasonable agreement with the adjusted R–squared ($R^2 = 0.9822$), thus, suggesting the reproducibility of the RSM model (Ohale et al. 2017; Onu et al. 2020, 2021a; Betiku et al. 2018). The adequacy of the quadratic model is evaluated using the normal plot of residuals shown in Fig. 4a**.** It was observed that the residuals sustain a close alignment with the normality line, thereby, confirming the normality of the residual points.

Conversely, the plot of residuals vs. predicted values shown in Fig. 4b illustrates the random positioning of residuals around the baseline. This observation is a further indication of the suitability and accuracy of the developed quadratic model. An indication for the signal-to-noise ratio is given by the adequate precision value (APR). According to Betiku et al. (2018), for a model to effectively navigate

the design space, an APR greater than 4.0 is required. Therefore, an APR of 40.789 recorded in this study (Table 5) indicates the occurrence of sufficient signals relative to the noise. Also, the obtained coefficient of variance (CV) value (3.07%) indicates that the quadratic model was satisfactorily reproducible, judging from the assertions made by Onu et al. (2021a). The effect of the respective model term on the overall removal efficiency prediction was demonstrated using the Pareto effect plot (Fig. 4c), while the influence of the corresponding factors was estimated using Eq. (33). Figure 4c shows that the Fe–CS dosage (x_2) sustained the greatest influence on the A–N removal efficiency, thus buttressing its (Fe-CS) adsorptive applicability.

$$\begin{aligned} &A-N \text{ rem. } (\%) \\ &= 45.7989x_1 - 449.7647x_2 + 9.5928x_3 + 148.8144x_4 \\ &\quad - 0.1576x_5 + 0.0794x_1x_3 - 0.0187x_1x_5 - 0.3096x_2x_3 \\ &\quad + 1.6374x_2x_4 + 0.1952x_2x_5 - 0.0296x_3x_4 - 3.5087\,x_1^2 \\ &\quad - 16.4300x_2^2 - 0.0101x_3^2 - 0.2362x_4^2 - 23591.2578 \end{aligned} \tag{32}$$

$$P_i = \left[\frac{b_i}{\sum b_i}\right] x100 \tag{33}$$

where b is the f-value for the respective model term.

ANN

The graphical expression for the topological analysis of ANN is presented in Fig. 5a–Fig. 5d and the data partitioning (as a training set and test set) was conducted to eliminate over-training and over parameterization (Ohale et al. 2017; Onu et al. 2021b). Based on the hidden neurons selection criteria described in ″ANN″ Section, seven hidden neurons emerged as the most appropriate, because they depicted the least root-mean-square error (RMSE = 0.3619) and highest correlation coefficient ($R^2 = 0.9981$) values (see Fig. 5e). Hence, the developed network was described as a 5–7–1 (five input neurons, seven hidden neurons, and one output neuron) ANN architecture. Furthermore, the correlation coefficients obtained from the regression plots were 0.9919, 0.9625, 0.9447, and 0.9686 for training, validation, testing, and overall data sets, respectively, evidence for a high correlation between experimental data and ANN predictions. The consistency of the training process was estimated using the validation performance plot shown in Fig. 5f**.** The best validation performance of the training network generated a mean square error of 1.5061E-04 at the 53rd epoch iteration. The negligible mean square error value recorded for the study suggests that the absence of any over-fitting difficulty within the network (Onu et al. 2021a; Nwadike et al. 2020). The estimated R^2 and adjusted R^2 of the ANN model were 0.9025 and 0.8945, respectively. This suggests that 90.25% of the variations in experimental and predicted values can be described by the ANN model. Significant R^2 value established for the ANN model illustrates its capability in capturing the nonlinear nature of the adsorptive process of A–N onto Fe–CS.

ANFIS

The Sugeno type ANFIS structure for five input parameters and one output variable generated by grid partitioning is displayed in Fig. S1 (Supplementary data). The ANFIS structure was designed using a hybrid learning procedure that incorporates the least square and gradient technique. To enhance the effectiveness of the system, the raw data were normalized using Eq. (5). Among the five tested membership functions (trimf, trapmf, gbellmf, gaussmf, and guass2mf), gaussmf was selected as the most suitable for the development of the fuzzy inference system (FIS). The ANFIS architecture and training parameters are listed in Table 6**.**

Plots of the experimental and predicted A–N removal rates against run numbers for training, testing, checking, and overall data set are illustrated in Fig. 6(a–d), respectively. The significant spread of the interwoven data depicted in these plots is indicative of a high correlation between experimental and ANFIS predicted data. Furthermore, the calculated values R^2 and adjusted R^2 of the overall model performance were 0.9998 and 0.9978, respectively. This high R^2 further gave credence to the ability of the ANFIS model in predicting the A–N adsorptive removal (Onu et al. 2021a). The adjusted R^2 value implies that the ANFIS model can describe 99.78% of the variability between the experimental and predicted values (Betiku et al. 2018).

Model appraisal analysis

The precision of established models (RSM, ANN, and ANFIS) in estimating the A–N removal was appraised by comparing their error variance using the models presented in Table 2 and the results are presented in Table 7. According to Betiku et al. (2018), the value of R should be greater than 0.8 for an effective correlation between experimental and predicted values. Hence, the high R values ($R > 0.95$) obtained for the three models indicate their significant applicability in predicting experimental values. Adjusted R^2 is applied for testing the extent of R^2 overestimation, and its values obtained for the three models were satisfactorily sufficient, thus, validating their importance in predicting the A–N adsorptive removal. AARE was used to estimate the mean relative error between the model

predictions and experimental values. However, the ANFIS model yielded negligible AARE values, a demonstration of its (ANFIS model) prediction accuracy and superiority over RSM and ANN. MPSED estimates the geometric error distribution of a system and allows for several degrees of freedom. The values of MPSED obtained for RSM, ANN, and ANFIS were 23.3%, 27.1%, and 0.03%, respectively, which demonstrates the high prediction accuracy of the ANFIS model in capturing the nonlinear nature of the adsorptive process. Low error magnitudes obtained by testing other statistical indicators (RMSE, SSE, SD, HYBRID) on the outputs (Table 7) further gave credence to the superiority of the ANFIS model in the data prediction accuracy of the present study.

In general, results obtained from statistical analysis indicate that ANFIS was the most effective model, while ANN was the least effective model in predicting the adsorptive removal of A–N from AWW onto Fe–CS. Thus, the prediction accuracy of the studied models followed the order: ANFIS > RSM > ANN. The results obtained here correlate favorably with the findings of Onu et al. (2020) and Dastorani et al. (2010).

Effect of process variables

Figure 7a and b presents the contour plots for the temperature-dosage, and temperature-concentration effects, respectively. Both figures illustrate the positive impact of temperature on the removal efficiency and the entire adsorptive process. At all levels of adsorbent dosage and effluent concentration, an increase in the system temperature resulted in a rapid removal rate, as depicted in the 2D contour plots of Fig. 7(a–d). Onu et al. (2021a, b), had earlier reported the augmentation of the adsorbate–adsorbent interaction rate and strengthening of the adsorbate ions' mobility due to temperature increase. This phenomenon explains the observed increase in the removal efficiency upon temperature increase; thus, an endothermic process. Figure 7(b–e) depicts the 3D surface plots for the pH-dosage, and pH-concentration effects, respectively. The figures demonstrated that pH has a prominent quadratic effect on the A–N removal. At any given adsorbent dosage, increasing the pH from 4.0 to 6.8 resulted in a rapid A–N removal rate. However, increasing pH beyond pH 6.8 decreased the A–N removal efficiency (see Fig. 7b and e). Under slightly acidic conditions (pH 4.0–6.8), high amounts of H + competes with the ionized ammonia (NH_4^+) for available adsorption sites on Fe–CS, thus resulting in a reduced.

removal rate. Similarly, from Eq. (34), it is evident that a large amount of NH_4^+ was converted to $NH_3.H_2O$ molecule in an alkaline medium. The production of non-ionized $NH_3.H_2O$ resulted in adsorption difficulties and reduced removal rate of A–N in alkaline medium.

$$NH_4^+ + OH^- \rightarrow NH_3.H_2O \quad (34)$$

The effect of initial concentration on the removal efficiency was studied via a variation in the A–N initial concentration from 1.75 to 87.25 mg/L (see supplementary material, Table S1). Figure 7(c–e) shows a continuous reduction in A–N removal efficiency due to a progressive increase in initial concentration. This trend is attributed to the increased occupation of readily available adsorption sites on the surface of Fe–CS. Conversely, the effect of Fe–CS dosage depicted a reverse trend (Fig. 7f), as more active sites were made available upon the Fe–CS dosage increase from 1.0 to 2.2 g. This increment subsequently enhanced the A-N removal efficiency, as demonstrated in Fig. 7f. Similar observations have been reported by other researchers (Ohale et al. 2020; Aniagor et al. 2018; Onu et al. 2021a, b; Okafor et al. 2015).

Process optimization

Four optimization techniques (RSM-GA, ANFIS-GA, ANN-GA, and RSM) were applied for optimizing the selected input variables (pH, dosage, concentration, temperature, and time) used for modeling the adsorptive process. The optimization is aimed at maximizing the A–N removal efficiency. The range of constraints used for genetic algorithm optimization is given in Eq. (35)–Eq. (39), while optimum values for A–N removal efficiency predicted by each method are given in Table 8. The graphical solutions for the RSM-GA, ANFIS-GA and ANN-GA optimization processes are given in Fig. 8 (a-c), respectively. Judging by the figures, the removal efficiency increased steadily in a stepwise order from generation G_1–G_{198} for RSM-GA; generation G_1–G_{110} for ANFIS-GA; and generation G_1–G_{182} for ANN-GA, and subsequently remained constant until termination of the process. Such observations suggest the absence of a probable crossover or mutation, with a substantive optimization effect within the parameters (Betiku et al. 2018, 2016).

Duplicate validation experiments were conducted at the predicted optimum conditions, and the average A–N removal efficiency was calculated and is recorded as actual removal efficiency in Table 8. ANFIS-GA gave the highest A–N removal efficiency prediction of 92.60% (at pH 6.5, 2.2 g, 18.8 mg/L, 317 K, and 156 min). The superiority of ANFIS-GA prediction performance over those of RSM-GA and ANN-GA is linked to their experimental data capturing accuracy. Therefore, regarding the quality and accuracy of the optimized process variables, the observed performance of the optimization techniques followed the trend: ANFIS-GA > RSM-GA > ANN-GA > RSM.

$$5.0 \le \mathrm{pH} \le 9.0 \tag{35}$$

$$1.0(g) \le \mathrm{Fe-CSdosage} \le 2.2(g) \tag{36}$$

$$16\left(\frac{\mathrm{mg}}{L}\right) \le A-N\mathrm{concentration} \le 73\left(\frac{\mathrm{mg}}{L}\right) \tag{37}$$

$$308(K) \le \mathrm{Temperature} \le 318(K) \tag{38}$$

$$60(\mathrm{min}.) \le \mathrm{time} \le 180(\mathrm{min}.) \tag{39}$$

Mechanistic modeling

The adsorption kinetic data interpretation from a mechanistic viewpoint is an important step in describing the sorption process, and the accurate identification of the predominant sorption mechanism is also paramount for design purposes (Ohale et al. 2020). Generally, for an adsorption system, the solute transfer mechanism is typically characterized by either boundary layer diffusion (film) or intraparticle diffusion (pore), or both. Meanwhile, the final adsorption stages are mostly regarded as the equilibrium step, provided the adsorptive.

process was sustained to the termination point (Onu et al. 2021b). The overall mechanism is usually controlled by the slowest occurring step during the adsorption process. Therefore, the effect of the final step (equilibrium stage), which is assumed to be rapid, is considered negligible (Aniagor et al. 2018). The data used in kinetic modeling was obtained by studying the temporal variation of adsorption capacity (qt) with time at different A–N concentrations (See supplementary material, Fig. S2). The different mechanistic models applied in the study (Table 3) were independently discussed in the preceding subsections.

Double exponential model (DEM)

The double exponential model (DEM) describes the mechanism of a sorption process in two-step kinetics. The first phase entails a rapid uptake of adsorbate involving external and internal diffusion. Afterward, a slow step controlled by intraparticle diffusion dominates the sorption mechanism, and finally, the process attains equilibrium. The DEM plot and extracted mechanistic parameters are given in Fig. 9a and Table 9, respectively. From the obtained parameters, the overall kinetic constants (K_{D1} and K_{D2}) for the rapid and slow steps were relatively identical. This indicates that both film and intraparticle diffusion influenced the adsorption of A–N from AWW using Fe–CS.

Weber–Morris intraparticle diffusion model

Weber–Morris plot (q_t vs. $t^{1/2}$) is presented in Fig. 9 (e), while the generated mechanistic parameters are presented in Table 9. Obtained results illustrated that three distinct regions were involved during the sorption mechanism. The first linear region of film diffusion was recorded within the sorption period of 0–90 min. This period was characterized by bulk diffusion of the A–N ions onto the external surface of Fe–CS active sites. The second stage of intraparticle diffusion was recorded within the sorption period of 91–178 min. This second stage was dominated by the distribution of the A–N ions onto the macropore, mesopore and micropores of Fe–CS active sites. The third stage (179–300 min) represents the equilibrium period. The high R^2 value (0.92–0.99) depicted by the model denotes a significant influence of both film and pore diffusion in the adsorption process. Similarly, the Weber–Morris adsorption capacity (q_{ipd}) was observed to increase with increasing A–N concentration, an indication of increased film diffusion resistance. The improved adsorption capacity is attributed to the presence of high A–N concentration, which provided a favorable driving force to the external mass transfer process (Dotto and Pinto 2012). Meanwhile, none of the trend lines crossed the point of origin (Fig. 9e), thus confirming the fact that both film and intraparticle diffusion contributed significantly to the adsorptive mechanism.

Liquid film diffusion model (LFDM) and Homogeneous solid diffusion model (HSDM)

To estimate the film diffusion coefficient (k_f) and the intraparticle diffusion coefficient (Ds), the experimental data of the first region of the Weber–Morris plot was fitted with the liquid film diffusion model, LFDM (Eq. 28), while the experimental data of the second region was fitted with the homogeneous solid diffusion model, HSDM (Eq. 29). The model plots are presented in Fig. 9b and c for LFDM and HSDM, respectively, while the estimated mass transfer coefficients (k_f and Ds) and the associated R^2 values are presented in Table 9. From the results, it was concluded that LFDM and HSDM produced a good fit ($R^2 > 0.96$) with the tested experimental data, thus illustrating the significance of both film and intraparticle diffusion in the adsorptive mechanism. Furthermore, the k_f values decreased with increasing A–N concentrations, an observation that corroborates the earlier obtained result of decreased and increased sorption rate and film diffusion resistance, respectively, due to increased A–N concentration. Conversely, a reverse trend was observed with the HSDM, where intraparticle diffusion coefficient (Ds) was noted to increase with increasing A–N concentration (Fig. 9c). This indicates a reduction in the

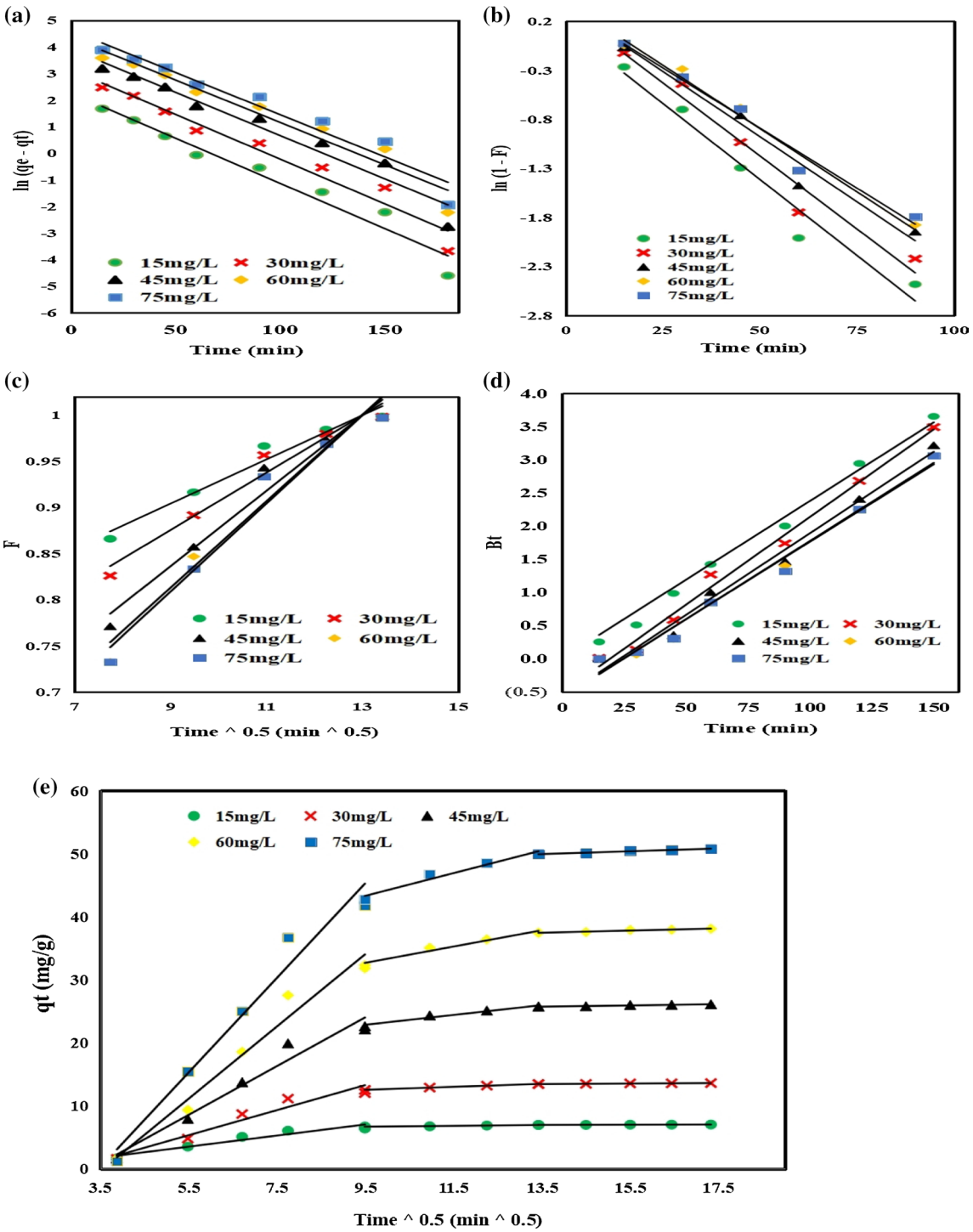

Fig. 9 Mechanistic model plot for **a** Double exponential model **b** Liquid film diffusion **c** Homogeneous solid diffusion model and **d** Boyd (Richenberg) model **e** Weber–Morris model

effect of the intraparticle diffusion mechanism as the A–N concentration increased. Similar observations have been reported by other researchers (Aniagor and Menkiti 2018; Dotto and pinto 2012).

Boyd (Richenberg) model

The contributions of film and intraparticle diffusion have been established in the previous discussion. However, none of the discussed models confirmed the actual

Table 9 Mechanistic parameters of studied models at varying concentrations of A–N

Models	15 mg/L	30 mg/L	45 mg/L	60 mg/L	75 mg/L
Double exponential model					
$D_{exp.1}$ (m^2/s)	2.1913	5.2731	11.4961	17.6318	23.2245
K_{D1} (L/g)	0.0342	0.0339	0.0329	0.0322	0.032
R_1^2	0.9484	0.9461	0.9381	0.9342	0.9312
$D_{exp.2}$ (m^2/s)	2.4121	5.8014	12.6341	19.3618	25.5006
K_{D2} (L/g)	0.0341	0.0337	0.0326	0.0319	0.0318
R_2^2	0.9585	0.9568	0.9507	0.9477	0.9452
Weber–Morris					
$K_{ipd\text{-}1}$ (mg/g/$min^{1/2}$)	0.8825	1.9909	3.8729	5.7414	7.5162
$q_{ipd\text{-}1}$ (mg/g)	0.0136	0.1024	0.2642	0.3103	0.3264
R_1^2	0.9262	0.9305	0.9601	0.9676	0.9655
$K_{ipd\text{-}2}$ (mg/g/$min^{1/2}$)	0.0677	0.2386	0.7818	1.2944	1.8061
$q_{ipd\text{-}2}$ (mg/g)	6.0135	10.243	15.415	20.386	26.1661
R_2^2	0.9418	0.9984	0.9621	0.9673	0.9584
$K_{ipd\text{-}3}$ (mg/g/$min^{1/2}$)	0.0156	0.0392	0.0989	0.1681	0.2242
$q_{ipd\text{-}3}$ (mg/g)	6.7287	12.9001	24.3841	35.1971	46.9211
R^2	0.952	0.952	0.952	0.9519	0.9519
Liquid film diffusion model					
K_{fd} (min^{-1})	0.031	0.0298	0.0266	0.0258	0.0245
R^2	0.9622	0.9618	0.9685	0.9782	0.977
Homogeneous solid diffusion model					
D_s (m^2/s)	5.03E–13	8.44E–13	1.46E–12	1.92E–12	2.0E–12
R^2	0.9627	0.9628	0.9626	0.9601	0.9629
Boyd (Richenberg) model					
B (min^{-1})	0.0238	0.0265	0.0247	0.0236	0.0234
R^2	0.9899	0.9901	0.9854	0.9852	0.9822

rate-controlling step involved in the adsorption of A–N onto Fe–CS. To determine the actual rate-controlling step, experimental data were further analyzed with Boyd kinetic model as done by other researchers (Aniagor and Menkiti 2018; Dotto and Pinto 2012; Tavliev et al. 2013). Boyd model [Eqs. (30) and (31)] and the model parameters obtained from the plot of Bt vs t is presented in Table 9. The linearity of the Boyd plot (Fig. 9d) was applied for determining the rate-controlling mechanism. The plot of Bt vs. t (at 15 mg/L A–N concentration) produced a straight line passing through the origin. Meanwhile, higher A–N concentrations (30 mg/L–75 mg/L) produced straight lines that did not pass through the origin. According to Tavlieva et al. (2013), if the plot of Bt vs. t produces a straight line passing through the origin, it illustrates an intraparticle diffusion mechanism; otherwise, film or external diffusion dominates. Hence, at a low A–N concentration (Conc. ≤ 15 mg/L), intraparticle diffusion dominated the adsorption process, while film diffusion mainly controlled the sorption process at higher concentrations (Conc.≥15 mg/L).

Thermodynamics

Thermodynamic studies were used to demonstrate the effect of change in temperature on the adsorption system (Ohale

Table 10 Thermodynamic parameters

Temperature		$-\Delta G^0$ kJ/mol	ΔH^0 kJ/mol	ΔS^0 J/mol k	E_A kJ/mol	R^2R^2
Deg. C	Deg. K					
30	303	2.8452				
35	308	2.9601	4.1150	22.971	3.7454	0.9531
40	313	3.0749				
45	318	3.1898				
50	323	3.3406				

et al. 2020). To illustrate this relationship, thermodynamic parameters such as a change in enthalpy (ΔH^0), change in Gibbs free energy (ΔG^0), change in entropy (ΔS^0), and activation energy (E_A) were calculated using Eqs. (40)–(43).

$$\ln(K_c) = \frac{\Delta S^0}{R} - \frac{\Delta H^0}{R}\frac{1}{T} \tag{40}$$

$$K_c = \frac{q_e}{C_e} \tag{41}$$

$$\ln(K_c) = \ln(A) - \frac{E_A}{\mathrm{RT}} \tag{42}$$

$$(\Delta G^0) = \Delta H^0 - T\Delta S^0 \tag{43}$$

From the plot of $\ln(K_c)$ vs. $\frac{1}{T}$, ΔH^0 and ΔS^0 were obtained from the slope and intercept, respectively. Calculated values of ΔH^0, ΔG^0, ΔS^0 and E_A are presented in Table 10. Positive ΔH^0 values showed that the adsorption process was endothermic. Also, negative ΔG^0 values indicate that the adsorption of A–N onto Fe–CS was spontaneous at all temperature levels. The reduction in ΔG^0 values with a corresponding increase in temperature depict improved adsorption rate at a higher temperature (Hashem et. al. 2021b).

The physisorption nature of the system was confirmed by the values of activation energy and enthalpy. According to Ohale et al. (2020) and Onu et al. (2021b), a physisorption process dominates if E_A the range between $0 < E_A < 40$ kJ/mol or if $\Delta H^0 < 80$kJ/mol. The values of E_A and ΔH^0 obtained in this work were 3.7454 kJ/mol and 4.1150 kJ/mol, respectively, which corroborates a physisorption process. The positive entropy value of 22.9710 kJ/mol indicates minor randomness around the surface of Fe–CS.

Limitations and recommendations for future studies

This study has modeled and optimized the adsorption of ammonia–nitrogen from abattoir wastewater. For accurate design and fabrication of adsorption tower, the results presented in this work are limited to the use of iron-functionalized crab shell as efficient adsorbent for high performance A-N removal. For more comprehensive treatment of AWW, additional developments in this research area are recommended as follows:

Taking into consideration the complex nature of AWW, a more robust optimization route such as multi-objective optimization is needed to include not just A-N, but other pollution control indices that are important for waste reduction from slaughterhouse industry. The GA optimization employed in this study considerably enhanced the efficiency of the A-N removal; however, more optimization algorithm such as particle swarm optimization, vector support mechanism, etc., is recommended.

Conclusion

The present study investigated the predictive accuracy of RSM, ANN, and ANFIS in modeling the adsorptive removal of A–N from AWW using novel Fe–CS prepared from CS. The characterization results established that the properties of CS were improved after chemical and thermal activation. The post-adsorption characterization demonstrated that Fe–CS was very effective in the adsorptive uptake of A–N. Experimental design illustrated the applicability of RSM, ANN and ANFIS in predictive modeling of A–N uptake from AWW. Model comparative analysis using statistical indices showed that the predictive accuracy of the studied models followed the order: ANFIS > RSM > ANN. Process optimization gave optimum values of 92%, 91.58%, 92.6%, and 91.8% for RSM–GA,

ANN–GA, ANFIS–GA and RSM, respectively. Results obtained from mechanistic modeling revealed that intraparticle diffusion dominated the adsorption process at a low concentration of A–N, while film diffusion mainly controlled the sorption process at A–N concentration higher than 15 mg/L. Thermodynamic parameters indicated that the process was spontaneous, physical, and endothermic.

Supplementary Information The online version contains supplementary material available at https://doi.org/10.1007/s13201-022-01713-4.

Author contributions All authors contributed to the study conception and design. Material preparation, data collection and analysis were performed by PEO, CEO, JTN, COA, CFO and NJO. The first draft of the manuscript was written by PEO and NJO, and all authors read, commented, and approved the final manuscript.

Funding This research work did not receive any specific grant from any agency in the public, commercial, or non-profit organization.

Declarations

Conflict of interest The authors declare that they have no bias or personal interest that could affect their actions during or after the course of review of this paper. All the authors involved have read and agreed on the final paper information before submission.

Ethical Approval Experimental design enhances environmental remediation processes by eliminating harmful wastes. All chemical wastes generated during this research were properly and safely disposed of.

References

Agarry SE, Owabor CN (2012) Evaluation of the adsorption potential of rubber (Hevea brasiliensis) seed pericarp-activated carbon in abattoir wastewater treatment and the removal of iron (iii) ions from aqueous solution. Niger J Technol 31(3):346–358

Agu CM, Menkiti MC, Ohale PE, Ugonabo VI (2020) Extraction modeling, kinetics, and thermodynamics of solvent extraction of Irvingia gabonensis kernel oil, for possible industrial application. Eng Rep. https://doi.org/10.1002/eng2.12306

American Public Health Association (APHA) (2005) Standard methods for the examination of water and wastewater. 18th ed. Washington, DC, 46

American Water Works Association (AWWA) (2005) Computer modeling of water distribution systems. Denver: AWWA.

Aniagor CO, Menkiti MC (2018) Kinetics and mechanistic description of adsorptive uptake of crystal violet dye by lignified elephant grass complexed isolate. J Environ Chem Eng. https://doi.org/10.1016/j.jece.2018.01.070

Arabameri M, Javid A, Roudbari A (2015) The use of artificial neural network (ann) for modeling of ammonia nitrogen removal from landfill leachate by the ultrasonic process. Int J Health Stud 1(3):13–19

Arslan A, Veli S (2011) Zeolite 13X for adsorption of ammonium ions from aqueous solutions and hen slaughterhouse wastewaters. J Taiwan Inst Chem Eng. https://doi.org/10.1016/j.jtice.2011.11.003

Atangana E, Chiweshe TT (2019) Metal adsorbance in abattoir wastewater using cross-linked chitosan derivatives. J Polym Environ 27(11):2624–2636

Betiku E, Odude VO, Ishola NB, Bamimore A, Osunleke AS, Okeleye AA (2016) Predictive capability evaluation of RSM, ANFIS and ANN: A case of reduction of high free fatty acid of palm kernel oil via esterification process. Energy Convers Manag 124:219–230. https://doi.org/10.1016/j.enconman.2016.07.030

Betiku E, Osunleke AS, Odude VO, Bamimore A, Oladipo B, Okeleye AA, Ishola NB (2018) Performance evaluation of adaptive neuro-fuzzy inference system, artificial neural network and response surface methodology in modeling biodiesel synthesis from palm kernel oil by trans-esterification. Biofuels. https://doi.org/10.1080/17597269.2018.1472980

Chen MJ, Chen KN, Lin CW (2015) Optimization on response surface models for the optimal manufacturing conditions of dairy tofu. J Food Eng 68:471–480

Chen Z, Wang X, Chen X, Chen J, Feng X, Peng X (2018) Nitrogen removal via nitritation pathway for low-strength ammonium wastewater by adsorption, biological desorption and denitrification. Bioresour Technol 267:541–549

Cheng H, Zhu Q, Xing Z (2019) Adsorption of ammonia nitrogen in low temperature domestic wastewater by modification bentonite. J Clean Prod 233:720–730

Couto RS, Oliveira AF, Guarino AWS, Perez DV, Marques MR (2016) Removal of ammonia nitrogen from distilled old landfill leachate by adsorption on raw and modified alumino-silicate. Environ Techno. https://doi.org/10.1080/09593330.2016.1212935

Dai L, Tan F, Li H, Zhu N, He M, Zhu Q, Hu G, Wang L, Zhao J (2017) Calcium rich biochar from the pyrolysis of crab shell for phosphorus removal. J Environ Manag 198:70–74

Dastorani MT, Moghadamnia A, Piri J et al (2010) Application of ANN and ANFIS models for reconstructing missing flow data. Environ Monit Assess 166:421–434

Dehghani MH, Yetilmezsoy K, Salari M et al (2019) Adsorptive removal of cobalt (II) from aqueous solutions using multi-walled carbon nanotubes and γ-alumina as novel adsorbents: modeling and optimization based on response surface methodology and artificial neural network. J Mol Liq. https://doi.org/10.1016/j.molliq.2019.112154

Dehghani MH, Karri RR, Yeganeh ZT, Mahvi AH, Nourmoradi H, Salari M, Zarei A, Sillanpää M (2020) Statistical modeling of endocrine disrupting compounds adsorption onto activated carbon prepared from wood using CCD-RSM and DE hybrid evolutionary optimization framework: comparison of linear vs non-linear isotherm and kinetic parameters. J Mol Liq 302:112526

Djonga WG, Noubissié E, Noumi GB (2019) Discoloration test of a slaughterhouse effluent by adsorption on two adsorbents produced from sawdust of Khaya senegalensis and Pinus sp. Results Eng 4:100068

Dotto GL, Pinto LAA (2012) Analysis of mass transfer kinetics in the biosorption of synthetic dyes onto Spirulina platensis nanoparticles. Biochem Eng J 68:85–90

Elemile OO, Raphael DO, Omole DO, Oloruntoba EO, Ajayi EO, Ohwavborua NA (2019) Assessment of the impact of abattoir effluent on the quality of groundwater in a residential area of Omu-Aran, Nigeria. Environ Sci Eur 31:16. https://doi.org/10.1186/s12302-019-0201-5

Halim AA, Aziz HA, Johari MAM, Ariffin KS (2010) Comparison study of ammonia and COD adsorption on zeolite, activated carbon and composite materials in landfill leachate treatment. Desalination 262(1–3):31–35

Hariram V, Bose A, Seralathan S (2019) Dataset on optimized biodiesel production from seeds of Vitis vinifera using ANN, RSM and ANFIS. Data Brief 25:104298

Haseena PV, Padmavathy KS, Rohit KP, Madhu G (2016) Adsorption of ammonium nitrogen from aqueous systems using chitosan-bentonite film composite. Procedia Technol 24:733–740

Hashem A, Okeil A, Fikry M, Aly A, Aniagor CO (2021a) Isotherm and kinetics parametric studies for aqueous Hg (II) uptake onto N-[2-(methylamino) ethyl] ethane-1, 2-diaminated acrylic fibre. Arab J Sci Eng 46(7):6703–6714

Hashem A, Aniagor CO, Hussein DM, Farag S (2021b) Application of novel butane-1, 4-dioic acid-functionalized cellulosic biosorbent for aqueous cobalt ion sequestration. Cellulose 28(6):3599–3615

Hodúr C, Bellahsen N, Mikó E, Nagypál V, Šereš Z, Kertész S (2020) The adsorption of ammonium nitrogen from milking parlor wastewater using pomegranate peel powder for sustainable water, resources, and waste management. Sustainability 12:4880

Jeon C (2015) Adsorption behavior of silver ions from industrial wastewater onto Immobilized crab shell beads. J Ind Eng Chem. https://doi.org/10.1016/j.jiec.2015.08.015

Jeon C (2019) Removal of Cr (VI) from aqueous solution using amine-impregnated crab shells in the batch process. J Ind Eng Chem 77:111–117

Jorgensen TC, Weatherley LR (2003) Ammonia removal from wastewater by ion exchange in the presence of organic contaminants. Water Res 37:1723–1728

Kiran TR, Rajput S (2011) An effectiveness model for an indirect evaporative cooling (IEC) system: comparison of artificial neural networks (ANN), adaptive neuro-fuzzy inference system (ANFIS) and fuzzy inference system (FIS) approach. Appl Soft Comput 1:3525–3533

Kizito S, Wu S, Kirui WK, Lei M, Lu Q, Bah H, Dong R (2015) Evaluation of slow pyrolyzed wood and rice husks biochar for adsorption of ammonium nitrogen from piggery manure anaerobic digestate slurry. Sci Total Environ 505:102–112

Li D, Zhou Y, Long Q, Li R, Lu C (2020) Ammonia nitrogen adsorption by different aquifer media: an experimental trial for nitrogen

removal from groundwater. Int J Human Ecol Risk Assess. https://doi.org/10.1080/10807039.2020.1768361
Lin Y, Li L, Hu J, Huang X, Zhou C, Jia M, Li Z (2014) Photometric determination of ammonia nitrogen in slaughterhouse wastewater with Nessler's reagent: effects of different pretreatment methods. Adv Mater Res 955–959:1241–1244
Lopes CL, de Assis TM, Passig FH, de Lima Model AN, Mees JBR, Cervantes FJ, Gotardo JT, Gomes SD (2022) Nitrogen removal from poultry slaughterhouse wastewater in anaerobic-anoxic-aerobic combined reactor: integrated effect of recirculation rate and hydraulic retention time. J Environ Manag 303: https://doi.org/10.1016/j.jenvman.2021.114162
Lyu H, Tang J, Cui M, Gao B, Shen B (2019) Biochar/iron (BC/Fe) composites for soil and groundwater remediation: synthesis, applications, and mechanisms. Chemosphere 246:125609. https://doi.org/10.1016/j.chemosphere.2019.125609
Mahanty S, Chatterjee S, Ghosh S, Tudu P, Gaine T, Bakshi M, Das P, Das S, Bhattacharyya S, Bandyopadhyay S, Chaudhuri P (2020) Synergistic approach towards the sustainable management of heavy metals in wastewater using mycosynthesized iron oxide nanoparticles: biofabrication, adsorptive dynamics and chemometric modeling study. J Water Process Eng 37:101426
Mao X, Xiong L, Hu X, Yan Z, Wang L, Xu G (2018) Remediation of ammonia contaminated groundwater in landfill sites with electrochemical reactive barriers: a bench scale study. Waste Manag 78:69–78
Mirahsani A, Sartaj M, Giorgi JB (2019) Assessment and optimization of total ammonia nitrogen adsorption in aqueous phase by sodium functionalized graphene oxide using response surface methodology. Environ Prog Sustain Energy 2019:1–10
Myers RH, Montgomery DC, Anderson-Cook C (2009) Response surface methodology: product and process optimization using designed experiments. John Wiley Sons, New York
Nwadike EC, Abonyi MN, Nwabanne JT, Ohale PE (2020) Optimization of solar drying of blanched and unblanched aerial yam using response surface methodology. Int J Trend Sci Res Develop 4(3):659–666
Ogbeide OA (2015) Meat industry development in nigeria: implications of the consumers' perspective. Mayfair J Agribus Manag 1:59–75
Ohale PE, Uzoh CF, Onukwuli OD (2017) Optimal factor evaluation for the dissolution of alumina from Azaraegbelu clay in acid solution using RSM and ANN comparative analysis. S Afr J Chem Eng 24:43–54
Ohale PE, Onu CE, Ohale NJ, Oba SN (2020) Adsorptive kinetics, isotherm and thermodynamic analysis of fishpond effluent coagulation using chitin derived coagulant from waste Brachyura shell. Chem Eng J Adv 4:100036
Okafor WC, Abonyi M, Okafor IOO, Ohale PE (2015) Comparative study of free amino nitrogen concentration in the fermentation of white and brown sorghum. J Basic Appl Res Int 13(1): 33–40. https://www.ikprress.org/index.php/JOBARI/article/view/3378
Okey-Onyesolu CF, Chukwuma EC, Okoye CC, Onukwuli OD (2020) Response surface methodology optimization of chito-protein synthesized from crab shell in treatment of abattoir wastewater. Heliyon 6(10):e05186
Onu CE, Igbokwe KP, Nwabanne JT, Charles OC, Ohale PE (2020) Evaluation of optimization techniques in predicting optimum moisture content reduction in drying potato slices. Artif Intell Agric 4:39–47
Onu CE, Nwabanne JT, Ohale PE, Asadu CO (2021a) Comparative analysis of RSM, ANN and ANFIS and the mechanistic modeling in eriochrome black-T dye adsorption using modified clay. S Afr J Chem Eng 36:24–42
Onu CE, Igbokwe PK, Nwabanne JT, Ohale PE (2021b) ANFIS, ANN, and RSM modeling of moisture content reduction of cocoyam slices. J Food Process Preserv 46:e16032
Panagopoulos A (2021) Energetic, economic and environmental assessment of zero liquid discharge (ZLD) brackish water and seawater desalination systems. Energy Convers Manag 235:1–11
Panagopoulos A (2022) Study and evaluation of the characteristics of saline wastewater (brine) produced by desalination and industrial plants. Environ Sci Pollut Res 29:23736–23749. https://doi.org/10.1007/s11356-021-17694-x
Qiang J, Zhou Z, Wang K, Qiu Z, Zhi H, Yuan Y, Zhang Y, Jiang Y, Zhao X, Wang Z, Wang Q (2020) Coupling ammonia nitrogen adsorption and regeneration unit with a high-load anoxic/aerobic process to achieve rapid and efficient pollutants removal for wastewater treatment. Water Res 170:115280
Qin L, He L, Yang W, Lin A (2020) Preparation of a novel iron-based biochar composite for removal of hexavalent chromium in water. Environ Sci Pollut Res. https://doi.org/10.1007/s11356-019-06954-6
Ren Z, Jia B, Zhang G, Fu X, Wang Z, Wang P, Lv L (2021) Study on adsorption of ammonia nitrogen by iron-loaded activated carbon from low temperature wastewater. Chemosphere 262:127895
Sajjadi B, Raman AAA, Parthasarathy R et al (2016) Sensitivity analysis of catalyzed-transesterification as a renewable and sustainable energy production system by adaptive neuro-fuzzy methodology. J Taiwan Inst Chem Eng 64:47–58
Sebestyén Z, Jakab E, Domán A, Bokrossy P, Bertóti I, Madarász J, László K (2020) Thermal degradation of crab shell biomass, a nitrogen containing carbon precursor. J Therm Anal Calorim 142:301–308. https://doi.org/10.1007/s10973-020-09438-9
Taheri M, Moghaddam MA, Arami M (2013) Technoeconomical optimization of Reactive Blue 19 removal by combined electrocoagulation/coagulation process through MOPSO using RSM and ANFIS models. J Environ Manag 128:798–806
Tavlieva MP, Genieva SD, Georgieva VG, Vlaev LT (2013) Kinetic study of brilliant green adsorption from aqueous solution onto white rice husk ash. J Colloid Interface Sci. https://doi.org/10.1016/j.jcis.2013.07.052
Ting WHT, Tan IAW, Salleh SF, Abdul WN (2020) Ammoniacal nitrogen removal by Eichhornia crassipes based phytoremediation: process optimization using response surface methodology. Appl Water Sci 10:80. https://doi.org/10.1007/s13201-020-1163-x
Tu Y, Feng P, Ren Y, Cao Z, Wang R, Xu Z (2019) Adsorption of ammonia nitrogen on lignite and its influence on coal water slurry preparation. Fuel 238:34–43
Vijayaraghavan K, Ni Winnie HY, Balasubramanian R (2011) Biosorption characteristics of crab shell particles for the removal of manganese(II) and zinc(II) from aqueous solutions. Desalination 266:195–200
Wang M, Xie R, Chen Y, Pu X, Jiang W, Yao L (2018) A novel mesoporous zeolite activated carbon composite as an effective adsorbent for removal of ammonia-nitrogen and methylene blue from aqueous solution. Bioresour Technol 268:726–732
Wang J, Zhang W, Kang X, Zhang C (2019) Rapid and efficient recovery of silverwith nanoscale zerovalent iron supported on high performance activated carbon derived from straw biomass. Environ Pollut 255:113043
Zarghi MH, Jaafarzadeh N, Roudbari A, Zahedi A (2020) Application of surface response method (RSM) to optimize of ammonia nitrogen removal from fresh leachate using combination of ultrasound and ultraviolet. Water Sci Technol. https://doi.org/10.2166/wst.2020.116/665489